Rare earth element partitioning between sulphides and melt: Evidence for Yb2+ and Sm2+ in EH chondrites

Nathan Ingrao, Tahar Hammouda, Maud Boyet, Marion Gaborieau, Bertrand Moine, Ivan Vlastélic, Mohamed Ali Bouhifd, Jean-Luc Devidal, O. Mathon, D. Testemale, et al.

Rare Earth Element Partitioning Between Sulphides and Melt: Evidence for Yb^{2+} and Sm^{2+} in EH Chondrites

N.J.Ingrao[a], T.Hammouda[a], M.Boyet[a], M.Gaborieau[a], B.N.Moine[b], I.Vlastelic[a], M.A. Bouhifd[a], J.-L. Devidal[a], O. Mathon[c], D.Testemale[d], J.-L. Hazemann[d] , O. Proux[e]

a) Laboratoire Magmas et Volcans UMR 6524, CNRS, OPGC and IRD UR 163, Université Clermont-Auvergne, 6 avenue Blaise Pascal, Campus les Cézeaux, 63178 Aubière, France

b) Université de Lyon, UJM Saint-Etienne, UBP, CNRS, IRD, Laboratoire Magmas et Volcans UMR 6524, 23 rue Dr. Paul Michelon, 42023 Saint Etienne, France

c) European Synchrotron Radiation Facility, 71, avenue des Martyrs, CS 40220, 38043 Grenoble Cedex 9, France

d) CNRS, Univ. Grenoble Alpes, Inst NEEL, F-38000 Grenoble, France

e) Observatoire des Sciences de l'Univers de Grenoble (OSUG), UMS 832 CNRS, Univ. Grenoble Alpes, F-38041 Grenoble, France

Corresponding author: Nathan Ingrao: nathan.ingrao@uca.fr

Abstract

We present the first complete dataset of partition coefficients of Rare Earth Elements (REE) between oldhamites or molten FeS and silicate melts. Values have been determined at 1300 and 1400°C from experiments on mixtures of a natural enstatite chondrite and sulphides powders (FeS or CaS) performed in evacuated silica tubes for different f_{O_2} conditions (from IW-6.9 to IW-4.1). Obtained REE partitioning values are between 0.5 and 5 for oldhamites and between 0.001 and 1 for FeS. In both sulphides, Eu and Yb are preferentially incorporated compared to neighbouring REE. X-ray Absorption Near Edge Structure measurements on Yb and Sm demonstrate the partial reduction to 2+ valence state for both elements, Yb reduction being more pronounced. Therefore, the Yb anomaly in the sulphides is interpreted to be an effect of the presence of Yb^{2+} in the system and the amplitude of the anomaly increases with decreasing oxygen fugacity. The obtained oldhamite/silicate melt partition coefficients patterns are unlike any of the observed data in natural oldhamites from enstatite chondrites and achondrites. In particular, the low values do not explain the observed enrichments in oldhamite crystals. However, positive Eu and Yb anomalies are observed in some oldhamites from EH chondrites and aubrites. We attribute these anomalies found in meteorites to the sole oldhamite control on REE budget. We conclude that the presence of positive Eu and Yb anomalies in oldhamites is a good indicator of their primordial character and that these oldhamites carry a condensation signature from a highly reduced nebular gas.

1. Introduction

Enstatite chondrites form a group of meteorites that have been considered as a potential representative primitive material for the Earth (Javoy, 1995, 2010; Boyet et al., 2018). This is because they display isotope similarities with Earth for many elements, such as O, N, Ca, Ti, Cr, Ni, Mo, Ru, Os (Clayton, 1993; Javoy et al., 1984; Trinquier et al., 2007, 2009; Meisel et al., 1996; Dauphas et al., 2004; Fischer-Gödde and Kleine, 2017). Recently Dauphas (2017) proposed that enstatite chondrite type material represents at least 70 % of the Earth's building blocks. On the basis of FeO content of the present-day mantle Clesi et al. (2016) proposed that the Earth could have been accreted from 85 to 90% of material similar to EH chondrite. The redox conditions of formation of these meteorites have been estimated by using Si content of the metal phase (Larimer and Buseck, 1974) as well as by electrochemical methods (Brett and Sato, 1984). All studies concluded that equilibrium conditions are very reducing, at least below IW-3 (IW refers to iron-wüstite equilibrium (Fe-FeO equilibrium)). Under these particular conditions, elements that are lithophile in the Earth mantle conditions tend to be siderophile and/or chalcophile (Lodders and Fegley, 1993; Gannoun et al., 2011). This is attested by the presence of various unusual sulphide phases in these rocks. Among these sulphides, oldhamites (CaS) contain large concentrations of actinides and lanthanides, resulting in about half the budget of Rare Earth Elements (REE) of these meteorites being in oldhamites (Crozaz and Lundberg ,1995; Gannoun et al., 2011; Barrat et al. 2011).

Enstatite chondrites are also considered as an analogue of bulk Mercury or at least a good sample of the feeding zone of Mercury (Lewis, 1972; Wasson, 1988; Malavergne et al., 2010; Ebel and Alexander, 2011; Ebel, 2017). This is because of the low FeO surface content of Mercury determined by spectroscopy or by the MESSENGER mission (Sprague and Roush, 1998; Robinson and Taylor, 2001; Warrel and Blewett, 2004; Murchie et al., 2015), its high Fe/Si ratio, the presence of Ca and Mg sulphides at its surface (Nittler et al., 2011; Weider et al., 2012; Zolotov et al., 2013), the similar volatiles abundance as in EC

(Evans et al., 2015; Ebel, 2017) and the C abundance at its surface (Peplowski 2016). All those features are attribute to the highly reducing conditions for the formation of Mercury (McCubbin et al., 2012; Namur et al., 2016).

The REE distribution in enstatite chondrites has been studied in order to discuss the processes of formation of these meteorites. On the basis of the high melting temperature of CaS (2450±50°C for pure oldhamite, Medvedev et al., 1979) and the similarities of REE patterns measured in oldhamites of enstatite chondrites and aubrites (reduced achondrites), several authors suggested that the oldhamites were relicts of solar nebula condensation that survived igneous processes (Kurat et al., 1992; Floss and Crozaz 1993; Lodders et al., 1993; Lodders, 1995, 1996b). On the other hand, textural evidences and some REE patterns in natural CaS crystals are in favour of an igneous origin (Floss and Crozaz, 1993; Piani, 2016; Wheelock, 1994).

Previous experimental studies have addressed the REE partitioning between sulphide phases (CaS or FeS, crystalline or molten) and silicate melt (Jones and Boynton, 1983; Lodders and Palme, 1989, 1990; Lodders et al., 1990; Lodders, 1995, 1996 a, b; Dickinson et al., 1990 a, b, c, 1991; Dickinson and McCoy, 1997; Wohlers and Wood, 2015; 2017). The obtained partition coefficients could not reproduce the high enrichment (100 to 1000 times CI) found in natural oldhamites from enstatite chondrites and achondrites (Wheelock et al., 1994, Larimer and Ganapathy, 1987; Lundberg and Crozaz, 1988; Crozaz and Lundberg, 1995; Hsu, 1998). In addition, none of these studies provided a complete dataset on REE partitioning. In order to gain further insight into REE behaviour at very reduced conditions we have determined sulphide/silicate partitioning for oxygen fugacities between IW-5 and IW-7. We report the first complete experimental determination of molten FeS/silicate melt and oldhamite/silicate melt REE partition coefficients. The newly obtained D values are used to discuss the REE budget in reduced meteorites (enstatite chondrites and aubrites). In addition, some samples have been studied using X-ray Absorption Near

Edge Structure (XANES) in order to determine the valence states of Yb and Sm at reducing conditions.

2. Methods

2.1 Experiments

Starting material was a natural equilibrated Enstatite Chondrite (Hvittis, EL6, composition given by Rubin, 1984). Fragments of Hvittis were ground in ethanol and doped with between 250 and 1000 ppm of the 14 REE. Doping was achieved with REE oxides dissolved in nitric acid. Firstly, the REE solution was evaporated. The solid residue was then mixed with the Hvittis powder in ethanol. The obtained powders were dried and mixed in ethanol with either CaS or FeS powders. The final mixture contained 50 wt.% of the doped chondrite and 50 wt.% of the sulphide.

All the powders were loaded in graphite crucibles that were placed in pure silica tubes of 10 centimetres length. The tubes were evacuated at between 10^{-2} and 10^{-4} mbar and heated at 200°C before and during pumping to evacuate adsorbed volatile elements. The powders were equilibrated at 1300°C or 1400°C from 1 to 160 hours in a vertical furnace with MoSi heating components. The zone of the tube containing the sample was placed in the hotspot of the furnace (about 3 cm long). The temperature at the top of the tube was 200°C below the temperature at the hotspot. The temperature values were chosen following McCoy et al. (1997; 1999), who showed that 1400°C is the optimal temperature for formation of large oldhamite grains for the analyses. These temperatures are close to those of the previous experimental studies from the literature. The experiments ended by quenching the tubes in air. Quenching in water was avoided in order to prevent tube breakage and potential sample dissolution. The graphite crucibles were extracted from the tube, mounted in resin and polished to ¼ µm grit using diamond suspension. In order to avoid sulphide loss during polishing, water was avoided and ethanol was used as a lubricant. Lubricant was used since dry polishing could have been

destructive by plucking out the sulphides. Details on the experiments are presented in Table 1. The pressure values presented in the table are the initial pressures during sealing of the tubes. Gas formation during heating resulted in pressure increase but it was not possible to estimate its value.

2.2 Determination of oxygen fugacity

For most of the samples, the intrinsic fO_2 values were determined using Si content of the metal phase in equilibrium with the silicate assemblage, taking in consideration the following equilibrium:

(1) $SiO_2 = Si + O_2$

At equilibrium we have

(2) $\Delta G = 0 = \Delta G^\circ + RT.lnK_{eq}$

with

(3) $Keq = \frac{a_{Si} \cdot f_{O_2}}{a_{SiO_2}}$

yielding

(4) $\Delta G° = \Delta_r H^\circ - T\Delta_r S^\circ = -RTln\frac{a_{Si} \cdot f_{O_2}}{a_{SiO_2}}$,

where ΔG° is the free energy change for the reaction, R the gas constant, T the temperature (in K), $\Delta_r H$ the enthalpy changes of the reaction, $\Delta_r S$ the entropy changes and the $^\circ$ represents the standard state.

Silicon activity in the metallic phase is calculated with:

(5) $a_{Si} = X_{Si}.\gamma_{Si}$

X_{Si} is the Si molar content of the metal and γ_{Si} its activity coefficient. We used coefficients in the Fe-Si system given by Yang et al. (2014) in order to calculate Si activities.

The samples containing enstatite and in some case silica, we considered that all experiments were close to silica saturation. Then we set $a_{SiO_2} \approx 1$ in the calculations.

The pressure effect on $\Delta G°$ is considered negligible.

We calculated $\Delta_r H^\circ$ and $\Delta_r S^\circ$ using the compilation of Robie and Hemmingway (1979). Then we calculated oxygen fugacity of the system as follows:

(6) $f_{O_2} = e^{\frac{\Delta G^\circ}{RT}} \cdot \frac{a_{SiO_2}}{a_{Si}}$

We express the oxygen fugacity relative to iron-wüstite (IW) buffer.

For that we calculate $f_{O2} - f_{O2(IW)}$ at the same temperature:

(7) $\log f_{O_2}(sample) = \log f_{O_2}(IW) + \Delta IW$

with

(8) $\log f_{O_2}(IW) = 6.57 - \frac{27215}{T} + 0.055 \times (-1)/T$

after Huebner (1971).

Calculated f_{O_2} values are presented in Table 1.

2.3 Major element analysis

Quantitative analyses of major elements have been obtained with a CAMECA SX100 electron microprobe. A 15 kV accelerating voltage and a beam current of 15 nA were used. A focused beam was used on crystals and metals whereas the beam was defocused to 10µm for the glasses. In silicates, oxygen was always estimated according to oxide stoichiometry. The standards were natural minerals or synthetic oxides for silicates, pyrite for Fe and S in sulphides and pure metals (Fe, Mn, Si, Mg, Ni, Cr) for metallic alloys. Carbon content in the

metal phase was calculated by deficit of the sum of the analysed elements to 100%. We found that the difference to 100% was close to C saturation in iron-nickel alloys (Paek and Pak, 2014), which is expected from experiments performed in graphite crucibles. For some experiments, we also determined C content by electron microprobe, as indicated in Table 2 and 3.

2.4 Trace element analysis

An Agilent 7500-cs induced coupled plasma spectrometer (ICP-MS) coupled with a Resonetics M-50 laser was used to determine trace element concentrations in the different phases. The laser was operated at 193 nm wavelength with a 2mJ energy, and 2Hz pulse frequency for samples with CaS and 4 Hz for samples with FeS. Laser spot size was between 12 and 33 µm depending on the nature of the phase and the sample. Ablation was done in pure He atmosphere for duration ranging between 40 and 60 seconds. Signal calibration was done with a NIST 610 glass standard (Gagnon et al., 2008). Different internal standards were used: Fe for the FeS and metals and Ca for the oldhamites and silicate glasses. To check accuracy NIST 612 and BCR glasses were used as secondary standards. These analyses were compared to reference values (Gagnon et al, 2008). Our measurements are in good agreement with Gagnon et al values with always less than 20% deviation (see supplementary material). The GLITTER software (Van Achetberg et al., 2001) was used for the trace-element data reduction. Detection limit was <1ppm for all elements, as determined from counting statistics on the samples. In the study of Gannoun et al. (2011), LA-ICPMS and SIMS methods were compared and it was found by repeated measurements that the two methods agreed within 6% for light REE and between 4% and 16% for heavy REE.

2.5 X-Ray Absorption Near Edge Spectroscopy (XANES)

X-Ray Absorption Near Edge Spectroscopy (XANES) was used to determine Ytterbium and Samarium valence states in the experiments with CaS, only. Ytterbium L3-edge absorption data were collected on the BM 23 beamline at European Synchrotron Radiation Facility (ESRF) using the microbeam setup (5µm x 5µm) in reflection mode (Cartier et al. 2015). The energy was scanned between 8.85 keV and 9.05 keV. For Yb absorption energy calibration we used Yb metal foil (Goodfellow), YbI_2 commercial powder (Sigma Aldrich) for the divalent state and Yb_2O_3 (Sigma Aldrich) for the trivalent state. We also analysed a natural apatite crystal. Across the scanned energy range, we also observed the Ho L2-edge absorption line at 8.919 keV.

Samarium L3-edge absorption data were collected on the CRG BM 16 FAME-UHD Beamline, also at ESRF. On this beamline the beam size is 100 µm x 300 µm (HxV, Full Width Half Maximum values) therefore it was not possible to analyse the phases (sulphide; glass) separately (crystal typical size of the order of 30 µm) and the analyses represent averages of the phases present in the samples. However, on BM 16, analysing crystals allow for scanning the fluorescent X-ray wavelengths, yielding very high spectral resolution for the XANES data (high-energy-resolution fluorescence detection or HERFD-XANES, Hazemann (2009); Proux (2017)), the energy bandwidth of the fluorescence detection (measured around 1.1eV) being smaller than the energy bandwidths of the electronic level involved in the absorption process. Moreover, this narrow energy bandwidth of the fluorescence detection system allows also to have Sm L3-edge spectra (≈6.716keV) free from the Nd L1-edge contribution (≈6.722keV), even if the Sm Lα1 fluorescence line selected (at 5.636keV) is close to the Nd fluorescence lines characteristic of the L1-edge (mainly Lβ3 at 5.829keV and Lβ4 at 5.723keV). The incident energy ranged between 6.70 keV and 6.74 keV and no other absorption line than that of Sm was observed. For Sm L3-edge absorption energy calibration we used Sm metal foils (Goodfellow): energy position of the first maximum of the first derivative Sm metal foil spectrum was set to 6.616 keV. SmI_2 commercial powder (Sigma Aldrich) for the divalent state and Sm_2O_3 (Sigma Aldrich) for the trivalent state were also studied as reference spectra.

Figure 1 presents standards analysis for Yb and Sm sessions. For both Yb and Sm, the standard analyses were performed on pellets composed of a mixture of BN and the standard using the transmission mode. For both elements the pellets contained 20 times more BN than standard powders. For the samples, measurements were performed on polished resin mounts in fluorescence mode. Before absorption data acquisition, X-Ray fluorescence maps were acquired (Figure 2) in order to locate the phases in the sample.

3. Results

3.1 Sample description

The samples from experiments with CaS in the starting powders are composed by an amorphous silicate glass (45 to 53 vol%) containing oldhamite crystals (30 to 50 µm corresponding to 30 to 38 vol%) and iron-nickel metal phase (5 to 30 µm corresponding to 14 to 17 vol%). Run 1263 contains quartz crystals (30 to 50 µm corresponding to 5 vol%). The samples from experiments with FeS in the starting powders are composed by an amorphous silicate matrix (7 to 11 vol%) containing molten FeS (37 to 47 vol%), an iron-nickel metal phase (5 to 30 µm corresponding to 13 to 20 vol%) and enstatite crystals (28 to 36vol%). Some of the metal nuggets are enclosed within the iron sulphide phase. Typical sample textures are illustrated on Figure 3. Table 1 presents the phase fractions in each experiment. The proportions were estimated by coupling major element mass balance and image analysis using FOAMS program (Shea et al, 2010).

3.2 Major element composition

The phase compositions are given in Tables 2 and 3 for experiments containing CaS and FeS, respectively.

3.2.1 Experiments with CaS:

The oldhamite phase is close to endmember composition with 91 to 94 wt.% CaS, 4 to 7 wt.% MgS and 3 wt.% FeS. The metal phase has an average composition of 82 wt.% of Fe, 4 to 7

wt.% of Ni and 3 to 12 wt.% of Si. The matrix is a quenched liquid silicate phase with CaO (20 to 25 wt.%) and MgO (18 to 20 wt.%) being the main cations with Al_2O_3 (3 wt.%) and S (2.08 to 6.69 wt.%) and small amount of FeO (around 0.5 wt.%). With increasingly reducing conditions, S content in the melt decreases.

3.2.2 Experiments with FeS

The FeS phase is close to endmember composition with 99.5 wt.% FeS and 0.5 wt.% MgS. The metal phase has an average composition of 80 to 91 wt.% of Fe, 1 to 3 wt.% of Ni and less than 1 wt.% of S and very small amount of Si (between 0.01 and 1 wt.%). For experiments with FeS the matrix contains CaO (5 to 12 wt.%), MgO (15 to 30 wt.%), Al_2O_3 (7 to 15 wt.%), S (0.26 to 5.56 wt.%) and a small amount of FeO (around 1 wt.%).

With increasingly reducing conditions, S content in the metal decreases while Fe and Si contents increase.

The pyroxene composition is close to enstatite end member.

3.3 Trace element composition

Laser analyses were obtained for all 14 lanthanides. The results are presented in Table 4 and 5 for CaS and FeS experiments, respectively. The average mass concentrations measured have been calculated for each element and each phase for the different samples. From these values the sulphide/silicate melt partition coefficients have been calculated for the samples. One sigma error is given in the tables for each series of values. Trace element Nernst partition coefficients (D= (wt.% element in the crystal)/ (wt.% element in the silicate melt)) are given in Tables 4 and 5 for oldhamites and FeS, respectively. The reported errors on Nernst coefficient values were calculated as

$$(9)\ \sigma = \left(\sqrt{\frac{\sigma_{sulfide}^2}{sulfide} + \frac{\sigma_{melt}^2}{melt}}\right) \times D$$

Figures 4 and 5 present REE partitioning data for oldhamites and FeS, respectively. Elements have been sorted according to their atomic number.

In the oldhamite/silicate melt system, light-REE (LREE) and heavy-REE (HREE) are moderately incompatible, whereas middle-REE (Sm and Gd) are moderately compatible. For oldhamite/silicate melt coefficients we note two groups of spectra, one group of three spectra with La<0.1 and one group of five spectra with 0.1<La<1. For FeS, all studied trace elements are incompatible in our experiments and FeS are depleted in HREE relative to LREE. We note positive anomalies for Eu and Yb partition coefficients in all experiments.

3.4 Ytterbium and Samarium valence state

XANES measurements at Yb and Sm L3-edge energy levels are presented in Figure 6. Measurements on the standards give the positions of the edges for 3+, 2+ and 0 valence states.

For Yb, oldhamites and glass show peaks corresponding to 3+ and 2+ valence states. The peak intensity for Yb^{2+} is higher for oldhamites than for glass, whereas the peak of Yb^{3+} is higher for the glass than for oldhamites, suggesting a preferential incorporation of Yb^{2+} in oldhamites compare to the glass.

As mentioned in the method section, for Sm the beam size was too large to analyse sulphide and the glass separately. Thus, the Sm L3-edge XANES spectra obtained are representative of the valence states of this element in the bulk sample with one small peak at the energy of Sm^{2+} absorption and a larger peak at the energy of Sm^{3+}. Here we cannot document Sm valence distribution between oldhamites and silicate melt. However, the data show the presence of both Sm^{2+} and Sm^{3+} in the samples.

4 Discussion

285 **4.1 Origin of D value variation**

286

287 As noted above, there is a clustering of oldhamite/melt partition coefficients with two sets of
288 values. Three mixtures of the same composition were used for the experiments with CaS.
289 Figure 7A shows the variation of the La D value for different samples as a function of the timing
290 interval between the date of the powder preparation and the date of experiment for experiments
291 containing CaS. We note that, for a given starting mixture, early experiments yield low D
292 values, whereas subsequent experiments yield high values. Therefore, we attribute the
293 clustering of the partition coefficient values to aging of the powders before loading in the silica
294 tubes. Figure 7B also shows the La/Lu ratio as a function of the age of the powder for
295 experiments with oldhamites. The $D_{oldhamite/melt}$ (La) / $D_{oldhamite/melt}$ (Lu) does not vary with the age
296 of the powders. The starting mixtures were analysed subsequently with a Thermo Scientific
297 FLASH 2000 NC Analyzer to determine the carbon, hydrogen and nitrogen content. From
298 hydrogen data we determined a water content of about 2 wt.% in the aged powder. Therefore,
299 it appears that water favours REE incorporation in oldhamite. Consequently, the lower values
300 are representative of the true values for REE partitioning between oldhamites and silicate melt.
301 However, water presence does not affect the fractionation between REE and all experiments
302 will be considered in the section below, dealing with anomalies.

303 In the case of FeS, we also note that D values increase with aging of the starting powders
304 (Figure 7C) but the $D_{Fes/melt}$ (La) / $D_{Fes/melt}$ (Lu) variation is more complex (Figure 7D). Overall
305 there is a slight increase of the ratio with time for which there is no simple explanation but we
306 note that the two most reduced experiments (f_{O_2} of IW-5.8) yield the highest $D_{Fes/melt}$ (La) /
307 $D_{Fes/melt}$ (Lu) ratios. The data of Lodders (1996) also show the same trend. Analyses show that
308 the powder contains about 2 wt.% water so in the same manner as for oldhamite we attribute
309 D (La) increase to water presence. Given the present data we cannot further discuss the effect
310 of water on REE fractionation.

311

312 **4.2 Comparison with previous experimental studies**

313 In Figure 8 we compare the newly obtained oldhamite/silicate melt and FeS/silicate melt
314 partitioning coefficients with literature data. Jones and Boynton (1983) studied La, Gd and Lu
315 partitioning between FeS, (Ca, Mg) S and a basaltic melt. Lodders (1996) study presents La,
316 Nd, Sm, Eu, Gd, Yb and Lu partitioning between oldhamite or Fes and a silicate melt at 1300°C
317 and reducing conditions (log fO_2= IW-3.97). Dickinson et al. (1997) treated partitioning of La,
318 Ce, Nd, Sm, Eu, Gd and Yb between (Ca, Mg) S melt and a silicate melt at 1200 and 1300°C.

319 Overall our results agree with data from the literature. Jones and Boynton (1983) and Lodders
320 (1996) found that the partition coefficients increased from La to Lu for oldhamites while they
321 decrease for FeS. Lodders (1996) also reported positive anomalies for Eu. The Yb anomaly in
322 oldhamites that is observed in the present study has not been discussed by Lodders (1996)
323 because the two neighbouring elements had not been measured (only Lu was measured).
324 Dickinson et al. (1997) who studied oldhamite/silicate melt partitioning found two types of REE
325 patterns in sulphides: patterns from “oldhamites with a high Ca” content have a positive Eu
326 anomaly and those from “oldhamites with a low Ca” content have a negative Eu anomaly.

327 Wohlers and Wood (2015; 2017) studied the effect of fO_2 on U, Th and REE partitioning
328 between silicate melt, and molten Fe-S alloys. Our partitioning data on FeS-bearing systems
329 are consistent with the trend shown in their study. There is a sharp increase in D values as
330 FeO content of the silicate melt drops below 1 mol%.

331

332 **4.3 Ytterbium and Samarium valence change with redox conditions**

333 XANES measurements show unequivocally that Yb and Sm occur under both 3+ and 2+
334 valence states in the experiments. For Yb, positive anomalies are always detected in
335 sulphide/silicate melt partition coefficients.

In more detail, we modelled the ideal 3+ REE partition coefficients values. For this we used the lattice strain model (Blundy and Wood, 1994) for the substitution of cation according to its radius and charge in a given crystalline lattice. The data were modelled using a Quasi-Newtonian algorithm. For this we used measured data except for Eu, Yb and Sm. According to Papike (2005) and to XANES data, the three elements are present, at least partly, under the 2+ valence state in the samples. The ionic radii used for the model calculations have been taken from Shannon (1976) database for 3+ cations with a coordination number of 6. The resulting model parameters are given in the supplementary material sectionWe then calculated ideal partitioning data for 3+ elements for each experiment. These values are compared to measured data from experiment 1244 in Figure 9. The modelled values are the ideal partitioning coefficients called D*.

For FeS, the lattice strain model is not relevant because the temperature of the experiments is higher than the FeS melting temperature. In the rest of this section, a qualitative estimation of the role of the fO_2 on REE partitioning between oldhamite and silicate melt and valence change is presented. The objective here is to estimate what controls the behaviour of Yb and Sm in the studied system.

From the lattice strain modelling, we calculated the D/D* ratios to model the magnitude of the anomalies. These values are presented in Table 6. Figure 10 shows the amplitude of the Yb and Sm oldhamite/silicate melt partitioning anomalies (expressed as D/D*) versus the oxygen fugacity. D/D* value for Yb increases from 1.77 to 2.65 as oxygen fugacity decreases. For Sm the anomalies are smaller (from 1.04 to 1.09) and the correlation between D/D* and fO_2 less pronounced. However, we note the two most reduced experiments have the highest D/D* values. These observations suggest that the magnitude of the anomalies in Yb or Sm, could be a tool to estimate redox conditions for very reducing systems such as the enstatite chondrites environment.

4.4 On the origin of oldhamites in aubrites and enstatite chondrites

The origin of oldhamites in enstatite chondrites and achondrites has been debated on the basis of several textural and chemical criteria. In order to discuss this origin, it is necessary to present the REE distribution in aubrites and enstatite chondrites. In both types of meteorites oldhamites are the principal carrier of REE with abundances around 100 times CI for enstatite chondrites and from 50 up to 1000 times CI for aubrites (Gannoun et al., 2011; Floss et Crozaz, 1993; Floss et al., 2001). In EH chondrites, enstatites are a secondary carrier of REE, with abundances between 1 and 10 times the CI of these elements, whereas other phases (such as niningerite, MgS) contain less than the CI abundances. In EL chondrites, the plagioclase is rich in Eu (up to 7 times CI) but not in the other REE (around 1 times CI or less), while the REE content of other phases is less than the CI abundances (Floss, 2001). In aubrites, alabandite and diopside both have up to 10 times the REE content of CI. The plagioclase is also a Eu carrier (6 to 10 times CI), whereas others REE are less abundant (Floss, 1993; Wheelock, 1994). In aubrites, enstatite and forsterite have low REE abundances, with less than 0.2 times CI in the former and below detection limit in the latter (Floss, 1993; Wheelock, 1994).

On the basis of the general shape of the REE pattern as well as the presence of anomalies in some elements, 8 patterns have been identified in oldhamites from EH chondrites, 2 in oldhamites from EL chondrites and 10 in oldhamites from aubrites (Gannoun, 2011; Floss et Crozaz, 1993; Floss et al., 2001; Wheelock, 1994). Four of the patterns found in aubrites are also observed in EH and 2 of these 4 patterns are observed in EL. One type of pattern, convex upward, with only a negative Eu anomaly, is found in EH, EL and aubrites. It corresponds to the metamorphic type E described as clusters of anhedral oldhamite crystals accreted on kamacite-troilite clasts (Gannoun et al., 2011). The pattern associated to C-D types is also observed in aubrites but not in EL. It corresponds to single crystals of oldhamite intermingled in kamacite-troilite clasts and metal sulphide spherules or to oldhamite crystals covered with kamacite veneer. Figure 11 summarizes the REE pattern reported for oldhamites in enstatite chondrites and in aubrites.

389 Considering that all available experimentally determined oldhamite/silicate melt partition
390 coefficients for the REE have values of 1 or less, it is clear that a simple oldhamite/silicate melt
391 equilibrium cannot explain the high REE abundances found in oldhamite from enstatite
392 chondrites and aubrites. Therefore, despite its refractory character, CaS cannot be a liquidus
393 phase in natural complex systems. In addition, the presence of FeS results in CaS-FeS eutectic
394 melting at about 1100 °C (Heumann, 1942). As discussed by previous authors, if oldhamite
395 were of magmatic origin in enstatite chondrites and aubrites, it should result from a complex
396 crystallisation history. Starting from a molten state with a chondritic REE abundance, enstatite
397 would crystallise first. The resulting liquid would therefore become enriched in REE. Upon
398 further cooling the sulphide phase (still molten) would be separated from the silicate phase.
399 Given the overall sulphide/silicate partition coefficient values, the two melts would have similar
400 concentrations for the light REE whereas the sulphide phase would be enriched in the heavy
401 REE. Given the Fe/Ca ratio of the sulphide phase (of the order of 20; Rubin 1984) FeS would
402 crystallise first according to the FeS-CaS phase diagram (Lodders 1996) and REE would stay
403 in the sulphide liquid. Finally, CaS would crystallise last, concentrating all REE from the
404 sulphide liquid. Given that oldhamite represents less than 1 wt% of enstatite chondrites,
405 enrichment by a factor of 100 is expected.

406 As an alternative, some have suggested that oldhamites represent a relict of the primitive
407 nebula and were not modified by interaction with other phases (Lodders, 1996; Dickinson and
408 McCoy, 1997). However, such scenario should result in positive Eu and Yb anomalies (as
409 discussed below), which are not commonly observed.

410 The present study provides the first analyses on Yb and Sm valence states in sulphides and
411 silicates equilibrated under reducing conditions, such as those relevant to enstatite chondrites
412 and aubrites. XANES analyses demonstrated the presence of Yb^{2+} and Sm^{2+}. Our results on
413 Ho showed no presence of Ho^{2+}. In the case of Yb, the micro-XANES data suggest preferential
414 partitioning of Yb^{2+} in the sulphide phase, compared to the silicate melt. We did not study Eu
415 valence state specifically, but we anticipate all Eu to be present in 2+ state, according to

previous works (Papike, 2005). The positive europium and ytterbium anomalies observed in the present experimental work as well as in some of the naturally occurring oldhamites can thus be attributed to the preferential incorporation of these elements in their divalent state in the CaS crystals. Moreover, it is also possible that Sm anomalies observed by Gannoun et al. (2011) could be due to reduction to Sm^{2+}. Our results suggest that Eu and Yb (and possibly Sm) anomalies are observed when oldhamite is the only phase controlling REE budget. Lodders (1996) and Dickinson and McCoy (1997) suggested that Eu and Yb anomalies are attributed to preferential evaporation and condensation of these REE. Here we see that reduction can be at the origin of these anomalies. The diversity of REE patterns necessitate that other processes are implied during CaS crystallisation (Lodders, 1996; Dickinson, 1997).

5 Conclusion

The sulphide/silicate melt REE partition coefficients obtained in the present experimental study as well as in previous ones do not reproduce the observed abundances of REE in sulphides of reduced chondrites (enstatite chondrites) and achondrites (aubrites). This is true for oldhamites (measured oldhamites REE contents are higher than predicted ones) as well as for FeS (measured FeS REE contents are below detection limits). However, the present study does reproduce europium and ytterbium anomalies that are observed in a large population of oldhamites from reduced chondrites and achondrites. The positive Eu and Yb anomalies in oldhamites are attributed to the presence of Eu^{2+} and Yb^{2+} as identified for the latter using XANES measurements.

As to what oldhamites can tell us about REE budget during condensation of the solar system depends on its primordial character. Our results strongly suggest that, only in case of presence of Eu and Yb positive anomalies, REE budget is directly and only controlled by oldhamite. Other oldhamites types appear to have been affected by secondary processes that may be magmatic or metamorphic. Primitive oldhamite crystals, that is those displaying Eu and Yb

positive anomalies, are found only in EH chondrites and in aubrites. All oldhamites from EL chondrites appear to have a complex history. Since primitive oldhamites REE abundances do not match the oldhamite/silicate melt partition coefficients it seems that their REE signature has been acquired by interaction with the nebular gas. Those crystals may therefore provide us with information about the primordial environment of the solar system.

ACKNOWLEDGEMENTS

We thank J.-M. Hénot for assistance using the SEM and Claire Fonquernie for the determination of the volatile content of the powders. This research was financed by the French Government Laboratory of Excellence initiative ANR-10-LABX-0006. The FAME-UHD project is financially supported by the French "grand emprunt" EquipEx (EcoX, ANR-10-EQPX-27-01), the CEA-CNRS CRG consortium and the INSU CNRS institute. This work was supported by the European Synchrotron Radiation Facility (proposals ES-369) and by the French CRG (proposal 16-01-784). This research received funding from the French PNP program (INSU-CNRS). This project has received funding from the European Research Council (ERC) under the European Union's Horizon 2020 research and innovation program (Grant Agreement No 682778 - ISOREE). We acknowledge the helpful comments by the anonymous reviewers and we thank the AE, W. van Westrenen, for handling the manuscript. This is Laboratory of Excellence ClerVolc contribution № 364.

460 **Table captions**

461 **Table 1:** Experimental conditions and run results.

462 **Table 2:** Major and minor electron microprobe composition of phases from experiments with
463 CaS.

464 **Table 3:** Major and minor electron microprobe composition of phases from experiments with
465 FeS.

466 **Table 4:** Minor and trace element concentrations in silicate melts and oldhamites in ppm from
467 experiments with CaS powders and corresponding Nernst oldhamites/melt REE partition
468 coefficients. All data were obtained by LA-ICP-MS.

469 **Table 5:** Minor and trace element concentrations in silicate melts and molten FeS in ppm from
470 experiments with FeS powders and corresponding Nernst molten FeS/melt REE partition
471 coefficients. All data were obtained by LA-ICP-MS.

472 **Table 6:** D/D* ratios calculated for oldhamite/melt partitioning experiments.

473

474

Figure captions

Fig. 1: X-ray absorption near-edge spectroscopy spectra of the standards used. For ytterbium: results for Yb L3-edge obtained on BM23 beamline at ESRF, using the microbeam setup. Note that Ho L2-edge absorption line is also visible. For samarium: Results for Sm L3-edge obtained on BM16 FAME-UHD beamline of ESRF-CRG.

Fig. 2: Fluorescence maps obtained at ESRF on BM 23 line showing S, Ca and Fe abundance, for sample 1250. Regions rich in Ca and S (in red and orange on the maps on the left) are oldhamites. The red region in the right bottom angle of the third map corresponds to an iron-nickel bead. Regions poorer in the three elements (blue in the S and Fe map and green in the Ca map) represent the quenched glass. A SEM picture of the same area is compared to the maps in the fourth panel. Oldh. = oldhamite crystals; Metal = Fe-Ni alloy, Melt = quenched silicate melt.

Fig. 3: SEM pictures of four samples representative of the observed phases assemblage **A.** Hvittis + CaS starting powder at 1300°C. **B.** Hvittis + CaS starting powder at 1400°C. **C.** Hvittis + FeS starting powder at 1300°C. **D.** Hvittis + FeS starting powder at 1400°C. Oldh. = oldhamite crystals; Metal = Fe-Ni alloy, Melt = quenched silicate melt; Enst.=enstatites.

Fig. 4: Rare Earth Elements oldhamite/silicate melt partition coefficients for all the experiments with Hvittis + CaS mixture.

Fig. 5: Rare Earth Elements FeS/silicate melt partition coefficients for all the experiments with Hvittis + FeS mixture.

Fig. 6: XANES spectra determined from Hvittis + CaS samples. **A.** Yb L3-Edge measured in the oldhamite crystals. **B.** Yb L3-Edge measured in the glasses **C.** Sm L3-Edge on bulk samples. In A. and B. Ho absorption-edge is visible at 8.919keV. The patterns correspond to an average of the data for each sample, with 3 to 19 analyses by element on different spots. For the Yb analyses on the sample 1244 only one spot in both oldhamites and the glass were analysed.

Fig. 7: Sulphide/melt partition coefficient values obtained in the present study plotted as a function of the age of the powders used, expressed in days. The three mixtures used are represented in grey, open, and closed symbols for powders 1, 2, and 3, respectively. **A.** La for oldhamite/silicate melt partitioning. **B.** La/Lu partition coefficient ratio for oldhamite/silicate melt system. **C.** La for FeS/silicate melt partitioning. **D.** La/Lu partition coefficient ratio for FeS/silicate melt system. All REE present the same pattern as that of La shown in A and C.

Fig. 8: Comparison of the partition coefficients obtained in the present study with literature values (Lodders, 1996; Dickinson et al., 1997; Jones and Boynton, 1983). **A.** Oldhamite/silicate melt data. **B.** FeS/silicate melt data.

Fig. 9: Experimental values for oldhamite/silicate melt REE partition coefficients for experiment 1244, compared to values obtained using the lattice-strain model (Blundy and Wood, 1994) and considering all REE in the 3+ valence states with a coordination number of 6.

Fig. 10: Intensities of the anomalies in Yb and Sm expressed as the ratio of measured and modelled partition coefficient (D/D*) plotted as a function of oxygen fugacity determined in the experiments.

Fig. 11: Various CaS REE patterns normalised to CI in aubrites and enstatite chondrites from the literature (Larimer and Ganapathy, 1987; Floss and Crozaz, 1993; Wheelock et al., 1994; Floss et al., 2001; Gannoun et al., 2011). Larimer and Ganapathy (1987) data shown as dashed line were obtained for 5 REE only. Other data cover all REE. See text for discussion and comparison with the present experimental data.

524 Barrat J.A., Zanda B., Bollinger C. and Liorzou C. (2011) Trace Element Geochemistry of
525 Enstatite Chondrites: The So-Called “Refractory Lithophile” Elements. *Meteoritics and*
526 *Planetary Science supplement* **74**, 5487.

527 Blundy J. and Wood B. (1994) Prediction of crystal-melt partition coefficients from elastic
528 moduli. *Nature* **372**, 452-454.

529 Boyet M., Bouvier A., Frossard P., Hammouda T., Garçon M. and Gannoun A. (2018)
530 Enstatite chondrites EL3 as building blocks for the Earth: The debate over the ^{146}Sm-^{142}Nd
531 systematics. *Earth and Planetary Science Letters* **488**, 68-78.

532 Brett S., and Sato M. (1983) Intrinsic oxygen fugacity measurements on seven chondrites,
533 a pallasite, and a tektite and the redox state of meteorite parent bodies. *Geochimica and*
534 *Cosmochimica Acta* **48**, 111-120.Cartier C., Hammouda T., Boyet M., Mathon O.,
535 Testemale D. and Moine B.N. (2015) Evidence for Nb^{2+} and Ta^{3+} in silicate melts under
536 highly reducing conditions: a XANES study. *American Mineralogist* **100**, 2152-2158.

537 Clayton R.N. (1993) Oxygen isotopes in meteorites. *Annual Review Earth Planet Sciences*
538 **21**, pp. 115-149.

539 Clesi V., Bouhifd M.A., Bolfan N., Manthilake G., Fabbrizio A. and Andrault D. (2016) Effect
540 of H2O on metal-silicate partitioning of Ni, Co, V, Cr, Mn and Fe: Implications for the
541 oxidation state of the Earth and Mars. *Geochimica and Cosmochimica Acta* **192**, 97-121.

542 Crozaz G. and Lundberg L.L. (1995) The origin of oldhamite in unequilibrated enstatite
543 chondrites. *Geochimica and Cosmochimica Acta* **59**, 3817-3831.

544 Dauphas N. (2017) The isotopic nature of the Earth's accreting material through time.
545 *Nature* **541**, 521-524.

546 Dauphas N., Davis A. M., Marty B., and Reisberg L. (2004) The cosmic molybdenum-
547 ruthenium isotope correlation. *Earth Planet. Sci. Lett.* **226**, 465-475.

548 Dickinson T.L. and McCoy T. (1997) Experimental rare-earth-element partitioning in
549 oldhamite: Implications for the igneous origin of aubritic oldhamite. *Meteoritics & Planetary*
550 *Science* **32**, 395-412.

551 Dickinson T.L., Lofgren G.E. and McKay G.A. (1990) REE partitionning between silicate
552 liquid and immiscible sulfide liquid: the origin of the negative Eu anomaly in Aubrite sulfides.
553 *Lunar and Planetary Science* **XXI**, 284-285.

554 Dickinson T.L., Lofgren G.E. and McKay G.A. (1990) Sulfide fractionation and the origin of
555 the negative Eu anomaly in aubrites. *Metoritical Society* **1990**, 358.

556 Dickinson T.L., McKay G.A. and Lofgren G.E. (1991) On the magmatic origin of oldhamite
557 in Aubrites. *Lunar and Planetary Science* **XXII**, 319-320.

558 Ebel, D. S. and Alexander, C. M. O'D. **(2011)**. Equilibrium condensation from chondritic
559 porous IDP enriched vapor: Implications for Mercury and enstatite chondrite origins.
560 *Planetary and Space Science* **59**, 1888–1894.

561 Ebel, D. S. and Stewart, S. T. **(2017)**. Chapter 18: The Elusive Origin of Mercury. in
562 *Mercury: The View after MESSENGER,* Cambridge University Press.

563 Evans L. G., Peplowski P. N., McCubbin F. M., McCoy T. J., Nittler L. R., Zolotov M. Yu.,
564 Ebel D. S., Lawrence D. J., Starr R. D., Weider S. Z. and Solomon S. C. (2015). Chlorine
565 on the surface of Mercury: MESSENGER gamma-ray measurements and implications for
566 the planet's formation and evolution. *Icarus* **257**, 417–427.

567 Fischer-Gödde M. and Kleine T. (2017) Ruthenium isotopic evidence for an inner Solar
568 System origin of the late veneer. *Nature* **541**, 525-527.

569 Fitoussi C. and Bourdon B. (2012) Silicon Isotope Evidence Against an Enstatite Chondrite
570 Earth. *Science* **335**, 1477-1480.

571 Floss C. and Crozaz G., (1993) Heterogeneous REE patterns in oldhamites from aubrites:
572 Their nature and origin. *Geochimica and Cosmochimica Acta* **57**, 4039-4057

573 Floss C., Fogel R.A., Lin Y. and Kimure M. (2003) Diopside-bearing EL6 EET 90102 :
574 Insights from rare earth element distributions. *Geochimica et Cosmochimica Acta* **67**, 543-
575 555.

576 Gagnon J.E., Fryze B.J., Samson I.M. and Williams-Jones A.E. (2008) Quantitative
577 analysis of silicate certified reference materials by LA-ICPMS with and without an internal
578 standard. *Journal of Analystical Atomic Spectrometry* **23**, 1529-1537.

579 Gannoun A., Boyet M., El Goresy A. and Devouard B. (2011) REE and actinide
580 microdistribution in Sahara 97072 and ALHA77295 EH3 chondrites: A combined
581 cosmochemical and petrologic investigation. *Geochimica et Cosmochimica Acta* **75**, 3269-
582 3289.

583 Hazemann J.-L., Proux O., Nassif V., Palancher H., Lahera E., Da Silva C., Braillard A.,
584 Testemale D., Diot M.-A., Alliot I., Delnet W., Manceau A., Gélébart F., Morand M.,
585 Dermigny Q., Shukla A. (2009) High Resolution Spectroscopy on an X-ray Absorption
586 Beamline. *J. Synchrotron Radiat.* **16,** 283-292

587 Heumann T. (1942) Die Löslichkeit von Eisensulfid in Kalziumsulfid bei der eutektischen.
588 *Temperatur. Archiv Eisenhuttenw* **15**, 557-558.

589 Hsu W. (1998) Geochemical and petrographic studies of oldhamite, diopside, and
590 roedderite in enstatite meteorites. *Meteorit. Planet. Sci.* **33**, 291-301.

591 Huebner J.S. (1971) *Buffering techniques for hydrostatic systems at elevated pressures.*
592 *Research techniques for high pressure and high temperature.* ed. G. C. Ulmer, 123-177.

593 Javoy M., Pineau F. and Demaiffe D. (1984) Nitrogen and carbon isotopic composition in
594 the diamonds of Mbuji Mayi (Zaïre). *Earth and Planetary Science Letters* **68**, 399-412.

595 Javoy M. (1995) The integral enstatite chondrite model of the Earth. *Geophysical Research*
596 *Letters* **22**, 2219-2222.

597 Javoy M., Kaminski E., Guyot F., Andrault D., Sanloup C., Moreira M., Labrosse S.,
598 Jambon A., Agrinier P., Davaille A. and Jaupart C. (2010) The chemical composition of the
599 Earth: Enstatite chondrite models. *Earth and Planetary Science Letters* **293**, 259-268.

600 Jones J. H. and Boynton W. V. (1983) Experimental Geochemistry in Very Reducing
601 Systems: Extreme REE Fractionation by Immiscible Sulfide Liquids. *Lunar and Planetary*
602 *Science* **XIV**, 353-354.

603 Kurat G., Zinner E. and Brandstätter F. (1992) An ion microprobe study of an unique
604 oldhamite-pyroxenite fragment from the Bustee aubrite. *Metoritical Society* **27(3)**, 246.

605 Larimer J.W. and Buseck P.R. (1974) Equilibration temperatures in enstatite chondrites.
606 *Geochimica et Cosmochimica Acta* **38**, 471-477.

607 Larimer J.W. and Ganapathy R. (1987) The trace element chemistry of CaS in enstatite
608 chondrites and some implications regarding its origin. *Earth and Planetary Science Letters*
609 **84**, 123-134.Lewis, J. S. (1972). Metal/silicate fractionation in the solar system. *Earth and*
610 *Planetary Science Letters.* **15**, 286–290.

611 Lodders K. and Fegley B.J. (1993) Lanthanide and actinide chemistry at high C / O ratios
612 in the solar nebula. *Earth and Planetary Science Letters* **117**, 125-145.

613 Lodders K. and Palme H. (1989) Europium anomaly produced by sulfide separation and
614 implications for the formation of Enstatite Achondrites. *Lunar and Planetary institute* **712**,
615 133-134.

616 Lodders K. and Palme H. (1990) Fractionation of REE during Aubrite formation: the
617 influence of FeS and CaS. *Lunar and Planetary Science* **XXI**, 710-711.

618 Lodders K. (1992) Lanthanide and Actinid condensation into oldhamite under reducing
619 conditions. *Lunar and Planetary institute* **23**, 797-798.

620 Lodders K. (1996) An experimental and theoretical study of rare-earth-element partitioning
621 between sulfides (FeS, CaS) and silicate and applications to enstatite achondrites.
622 *Meteoritics & Planetary Science* **31**, 749-766.

623 Lodders K. (1996) Oldhamite in enstatite achonrdites (Aubrites). *Proc. NIPR Symp.*
624 *Antarct. Meteorites* **9**, 127-142.

625 Lodders K. (2003) Solar System abundances and condensation temperatures of the
626 elements. *The Astrophysical Journal* **591**, 1220-1247.

627 Lundberg L.L. and Crozaz G. (1988) Enstatite Chondrites: A preliminary Ion Microprobe
628 study. *Metoritical Society* **1988 (23O)**, 285-286.

629 Malavergne, V., Toplis, M. J., Berthet, S. and Jones J. (2010). Highly reducing conditions
630 during core formation on Mercury: Implications for internal structure and the origin of a
631 magnetic field. *Icarus* **206**, 199–209

632 McCoy T.J., Dickinson T.L. and Lofgren G.E. (1997) Partial melting of the Indarch (EH4)
633 meteorite from 1000-1425C: New insights into igneous processes in enstatite meteorite.
634 *Lunar and Planetary Science* **XXVIII**.

635 McCoy T.J., Dickinson T.L. and Lofgren G.E. (1999) Partial melting of the Indarch (EH4)
636 meteorite: A textural, chemical, and phase relations view of melting and melt migration.
637 *Meteoritics & Planetary Science* **34**, 735-746.

638 McCubbin, F. M., Riner, M. A., Vander Kaaden, K. E. and Burkemper L. K. (2012). Is
639 Mercury a volatile-rich planet? *Geophysical Research Letters* **39**, L09202.

640 Medvedev V.A., Berman G.A., Gurvich L.V., Yungman V.S., Vorobiev A.F. and Kolesov
641 V.OP. (1979) Thermicheskie Konstanty Veschastv (Thermal Constants of Substances),
642 Be, Mg, Ca, Sr, Ba, Ra. *Ed V.P. Gluslko* (**Part IX**). 522.

643 Meisel T., Walker R.J. and Morgan J.W. (1996) The osmium isotopic composition of the
644 Earth's primitive upper mantle. *Nature* **383**, 517-520.

645 Murchie, S. L., Klima, R. L., Denevi, B. W., Ernst, C. M., Keller, M. R., Domingue, D. L.,
646 Blewett, D. T., Chabot, N. L, Hash, C. D., Malaret, E., Izenberg, N. R., Vilas, F., Nittler, L.
647 R., Gillis-Davis-J. J., Head, J. W. and Solomon, S. C. (2015). Orbital multispectral mapping
648 of Mercury with the MESSENGER Mercury Dual Imaging System: Evidence for the origins
649 of plains units and low-reflectance material. *Icarus* **254**, 287–305.

650 Namur, O., Charlier, B., Holtz, F., Cartier, C. and McCammon, C. (2016). Sulfur solubility
651 in reduced mafic silicate melts: Implications for the speciation and distribution of sulfur on
652 Mercury. *Earth and Planetary Science Letters* **448**, 102–114.

653 Nittler, L. R., Starr, R. D., Weider, S. Z., McCoy, T. J., Boynton, W. V., Ebel, D. S., Ernst,
654 C. M., Evans, L. G., Goldsten, J. O., Hamara, D. K., Lawrence, D. J., McNutt, R. L. Jr.,
655 Schlemm, C. E. II, Solomon, S. C. and Sprague, A. L. (2011). The major-element
656 composition of Mercury's surface from MESSENGER X-ray spectrometry. *Science* **333**,
657 1847–1850.

658 Paek M.-K. and Pak J.-J. (2014) Carbon solubility in liquid iron containing V, Mo and Ni.
659 *Materials transactions* **55**, 610-615.

660 Papike J.J., Karner J. and Shearer C.K. (2005) Comparative planetary mineralogy: Valence
661 state partitioning of Cr, Fe, Ti, and V among crystallographic sites in olivine, pyroxene, and
662 spinel from planetary basalts. *American Mineralogist* **91 (Issue 2-3)**, 277-290.

663 Piani L., Marrocchi Y., Libourel G. and Tissandier L. (2016) Magmatic sulfides in the
664 porphyritic chondrules of EH enstatite chondrites. *Geochimica et Cosmochimica Acta* **195**,
665 84-89.

666 Peplowski, P. N., Klima, R. L., Lawrence, D. J., Ernst, C. M., Denevi, B. W., Frank, E. A.,
667 Goldsten, J. O., Murchie, S. L., Nittler, L. R. and Solomon, S. C. (2016). Remote sensing
668 evidence for an ancient carbon-bearing crust on Mercury, *Nature Geoscience* **9**, 273–276.

669 Proux O., Lahera E., Del Net W., Kieffer I., Rovezzi M., Testemale D., Irar M., Thomas S.,
670 Aguilar-Tapia A., Bazarkina E. F., Prat A., Tella M., Auffan M., Rose J., Hazemann J.-L.
671 (2017) High Energy Resolution Fluorescence Detected X-ray Absorption Spectroscopy: a
672 new powerful structural tool in environmental biogeochemistry sciences. *Journal of*
673 *Environmental Quality* **46,** 1146-1157. Robie R.A., Hemingway B.S. and Fisher J.R. (1979)
674 Thermodynamic Properties of Minerals and Related Substances at 298.15 K and 1 Bar
675 Pressure and at Higher Temperatures. *U.S Geological Survey* **1452**.

676 Robinson, M. S. and Taylor, G. J. (2001). Ferrous oxide in Mercury's crust and mantle.
677 *Meteoritical and Planetary Science* **36**, 841–847.

678 Rubin A.E. (1984) Impact melt-rock clasts in the Hvittis enstatite chondrite breccia:
679 implications for a genetic relationship between EL chondrites and aubrites. *Journal of*
680 *geophysical research* **88**, 293-300.Shannon R.D., (1976) Revised Effective Ionic Radii and
681 Systematic Studies of Interatomic Distances in Halides and Chalcogenides. *Acta Cryst.* **32**,
682 751.

683 Shea T., Houghton B.F., Gurioli L., Cashman K.V., Hammer J.E. and Hobden B.J. (2010)
684 Textural studies of vesicles in volcaninc rocks: An integrated methodology. *Journal of*
685 *Volcanology and Geothermal Research* **190**, 271-289.

686 Sprague, A. L. and Roush, T. L. (1998). Comparison of laboratory emission spectra with
687 Mercury telescopic data. *Icarus* **133**, 174–183.Trinquier A., Birck J.-L. and Alle C.J., (2007)

688 Widespread 54 Cr heterogeneity in the inner Solar System. *The Astrophysical Journal* **655**,
689 1179-1185.

690 Trinquier A., Elliott D., Ulfbeck D., Coath C., Krot A.N. and Bizzarro M. (2009) Origin of
691 Nucleosynthetic Solar Protoplanetary Disk. *Science* **324**, 374-376.

692 Van Achterbergh E., Ryan C. G., Jackson S. E. and Griffin W. L. (2001) LA-ICP-MS in the
693 Earth Sciences - Appendix 3, data reduction software for LA-ICP-MS. in *Sylvester, P. J.,*
694 *ed., Short Course* **29**, St.John's Mineralogical Association of Canada, 239-243.

695 Warrell, J., and D. T. Blewett (2004), Properties of the Hermean regolith: V. New optical
696 reflectance spectra, comparison with lunar anorthosites, and mineralogical modeling,
697 *Icarus* **168**, 257–276

698 Wasson, J. T. and Kallemeyn, G. W. (1988). Composition of chondrites. *Philosophical*
699 *Transactions of the Royal Society of London A* **325**, 535–544.

700 Weider, S. Z., Nittler, L. R., Starr, R. D., McCoy, T. J., Stockstill-Cahill, K. R., Byrne, P. K.,
701 Denevi, B. W., Head, J. W. and Solomon, S. C. (2012). Chemical heterogeneity on
702 Mercury's surface revealed by the MESSENGER X-Ray Spectrometer. Journal of
703 Geophysical Research **117**, E00L05.

704 Wheelock M.M., Keil K., Floss C., Taylor G. and Crozaz G. (1994) REE geochemistry of
705 oldhamite-dominated clasts from the Norton County aubrite: Igneous origin of oldhamite.
706 *Geochimica et Cosmochimica Acta* **58**, 449-458.

707 Wohlers A. and Wood B. J. (2015) A Mercury-like component of early Earth yields uranium
708 in the core and high mantle ^{142}Nd. *Letter to Nature* **520**, 337–340.

709 Wohlers A. and Wood B. J. (2017) Uranium, thorium and REE partitioning into sulfide
710 liquids: Implications for reduced S-rich bodies. *Geochimica et Cosmochimica Acta* **205**,
711 226–244.

712 Yang X.-M., Li J.-Y., Li P.-C., Zhang M. and Zhang J. (2014) Determination of Activity
713 Coefficients of Elements and Related Thermodynamic Properties of Fe Si Binary Melts
714 Based on the Atom Molecule Coexistence Theory. *Steel Research international* **85**, 164-
715 206.

716 Zolotov, M. Yu., Sprague, A. L., Hauck, S. A., II, Nittler, L. R., Solomon, S. C. and Weider, S.
717 Z. (2013). The redox state, FeO content, and origin of sulfur-rich magmas on Mercury. *Journal*
718 *of Geophysical Research: Planets* **118**, 138–146.

Table

Table 1: Experimental conditions and run results.

Run	Powder	P(bar)	T(C)	Duration(h)	ΔIW	Result[a]
1250	EC + CaS	0.015	1300	10	-6.6	CaS (51). Met (15).Liq (34)
1263	EC + CaS	0.0075	1300	96	-6.5	CaS (52). Met (14).Liq (29).Qz(5)
1208	EC + CaS	0.009	1400	8	-6.9	CaS (46). Met (17).Liq (37)
1240	EC + CaS	0.0095	1400	10	-6.2	CaS (50). Met (15).Liq (35)
1246	EC + CaS	0.002	1400	48	-6.2	CaS (55). Met (15).Liq (30)
1305	EC + CaS	0.0034	1400	72	-6.1	CaS (51). Met (14).Liq (35)
1244	EC + CaS	0.009	1400	96	-5.8	CaS (46). Met (16).Liq (38)
1304	EC + CaS	0.0034	1400	160	-6.2	CaS (53). Met (14).Liq (33)
1266	EC + FeS	0.085	1300	1	-4.1	FeS (37). Met (20).Liq (7).Enst (36)
1282	EC + FeS	0.0007	1300	10	-4.5	FeS (45). Met (15).Liq (9).Enst (33)
1207	EC + FeS	0.009	1400	1	-4.8	FeS (45). Met (15).Liq (11).Enst (29)
1239	EC + FeS	0.0085	1400	1	-4.8	FeS (45). Met (14).Liq (13).Enst (28)
1284	EC + FeS	0.0007	1400	1	-5.8	FeS (47). Met (14).Liq (8).Enst (31)
1252	EC + FeS	0.01	1400	96	-5.8	FeS (47). Met (13).Liq (11).Enst (29)

Liq=Silicate melt ; Enst=Enstatite ; Met=Metallic Alloy ; CaS=Oldhamite ; FeS=molten FeS ; Qz=Quartz

[a] Phase proportions are expressed in volume percent

Table 2: Major and minor electron microprobe composition of phases from experiments with CaS.

Run	1250	Na 5	1263	Na 5	1208	Na 6	1240	Na 4	1246	Na 2	1305	Na 5	1244	Na 3	1304	Na 5
Oldhamite (wt%)		1σ		1σ		1σ		1σ		1σ		1σ		1σ		1σ
Si	0.07	0.02	0.07	0.03	0.07	0.06	0.43	0.52	0.02	0.01	0.01	0.01	0.05	0.02	0.02	0.01
Ti	0.01	0.01	0.01	0.01	2.24	0.06	0.00	0.00	0.01	0.01	0.02	0.02	0.00	0.00	0.01	0.02
Al	0.00	0.00	0.01	0.01	0.00	0.00	0.04	0.05	0.00	0.00	0.00	0.00	0.00	0.00	0.00	0.00
Cr	0.08	0.02	0.09	0.03	0.00	0.00	0.08	0.02	0.06	0.02	0.02	0.01	0.05	0.02	0.11	0.02
Fe	0.88	0.05	1.85	0.05	0.63	0.06	1.64	0.16	1.11	0.07	1.86	0.22	1.61	0.06	2.54	0.14
Mn	0.06	0.01	0.09	0.04	0.01	0.00	0.16	0.00	0.07	0.03	0.1	0.01	0.09	0.03	0.17	0.02
Mg	3.20	0.07	2.37	0.06	2.24	0.06	2.22	0.16	2.53	0.04	2.35	0.02	1.67	0.01	3.34	0.08
Ca	45.48	0.11	48.58	1.01	50.38	0.20	48.71	2.23	49.48	0.26	48.57	0.27	50.36	0.29	46.32	0.45
Na	0.05	0.02	0.02	0.01	0.02	0.02	0.07	0.11	0.01	0.01	0.01	0.01	0.00	0.01	0.00	0.00
Ni	0.01	0.01	0.03	0.02	0.09	0.01	0.00	0.00	0.02	0.03	0.02	0.01	0.02	0.02	0.01	0.02
S	50.16	0.16	43.46	0.46	44.21	0.13	41.73	2.57	43.84	0.14	43.72	1.3	43.4	0.15	42.96	0.12
Total	100.0		96.57		99.87		95.09		99.34		96.68		97.26		95.48	

Run	1250	Na 10	1263	Na 5	1208	Na 8	1240	Na 5	1246	Na 5	1305	Na 5	1244	Na 3	1304	Na 13
Metal (wt%)		1σ		1σ				1σ		1σ		1σ		1σ		1σ
Si	5.16	0.45	2.77	0.98	11.02	1.48	7.18	0.25	7.32	0.74	5.19	0.85	3.7	1.08	6.16	0.41
Al	0.00	0.00	n.a		n.a		n.a		n.a		n.a		n.a		0.00	0.00
Cr	0.25	0.18	n.a		n.a		n.a		n.a		n.a		n.a		0.03	0.03
Fe	84.62	0.73	85.58	2.48	79.99	2.74	83.88	1.38	82.33	5.59	85.44	2.82	83.02	1.93	86.18	1.24
Mn	0.01	0.02	0.02	0.02	0.01	0.02	0.02	0.01	0.01	0.01	0.00	0.00	0.00	0.00	0.01	0.02
Mg	0.01	0.01	0.00	0.00	n.a		0.01	0.01	0.03	0.01	0.01	0.01	0.01	0.01	0.00	0.01
Ca	0.35	0.11	0.24	0.18	n.a		n.a		0.00	0.00	n.a		n.a		0.35	0.11
Ni	5.94	0.73	6.95	0.35	4.36	1.22	6.19	0.17	5.42	0.49	6.16	0.3	7.31	0.56	6.34	0.16
S	0.65	0.78	0.54	0.89	0.23	0.28	0.20	0.12	0.81	1.69	0.27	0.37	0.38	0.13	0.06	0.10
C	2.91	1.15	n.a		n.a		n.a		n.a		n.a		n.a		1.63	1.52
Total	99.88		96.1		95.61		97.48		95.92		97.07		94.41		100.76	
C$^{\alpha}$	3.01		3.90		4.39		2.52		4.08		2.93		5.59		0.87	

Run	1250	Na 9	1263	Na 5	1208	Na 5	1240	Na 2	1246	Na 5	1305	Na 5	1244	Na 3	1304	Na 9
Silicate melt (wt%)		1σ		1σ				1σ		1σ		1σ		1σ		1σ
SiO_2	56.02	0.96	57.17	0.35	54.73	0.38	55.34	0.16	55.78	1.03	58.68	0.29	55.05	0.31	58.08	1.15
TiO_2	0.17	0.03	0.13	0.02	0.11	0.02	0.12	0.08	0.20	0.03	0.25	0.02	0.13	0.03	0.16	0.03
Al_2O_3	3.01	0.16	2.17	0.02	2.85	0.1	2.52	0.09	2.53	0.07	3.43	0.07	2.43	0.09	2.44	0.21
FeO	0.28	0.05	0.47	0.08	0.28	0.05	0.53	0.05	0.44	0.13	0.22	0.03	0.56	0.16	0.34	0.59
MnO	0.01	0.01	0.01	0.01	0.01	0.01	0.00	0.00	0.02	0.01	0.01	0.01	0.02	0.02	0.01	0.01
MgO	17.95	0.65	19.24	0.27	16.73	0.37	15.39	0.19	18.98	0.28	19.85	0.21	14.29	0.33	25.37	2.28
CaO	18.85	0.41	23.43	0.57	21.56	0.77	22.47	0.73	18.76	0.77	15.8	0.3	24.15	0.27	12.01	2.35
Na_2O	0.03	0.03	0.02	0.01	0.01	0.01	0.02	0.03	0.01	0.01	0.00	0.00	0.01	0.02	0.01	0.01
K_2O	0.02	0.01	0.02	0.01	0.00	0.00	0.02	0.01	0.01	0.01	0.01	0.01	0.02	0.02	0.00	0.01
Ni_2O_3	0.01	0.01	0.01	0.01	0.01	0.01	0.04	0.02	0.02	0.02	0.01	0.02	0.00	0.01	0.00	0.01
S	3.22	1.29	2.33	0.23	3.41	0.58	5.73	0.06	5.08	0.80	1.97	0.59	6.69	0.38	2.08	0.97
Total	99.57		105.00		99.7		102.18		101.83		100.23		103.35		100.50	

Na = Number of analyses

n.a Not analysed

a Maximum content calculated by difference from the total

O content in melt was estimated by stoichiometry

Table

Table 3: Major and minor electron microprobe composition of phases from experiments with FeS.

Run	1266	Na 5	1282	Na 5	1207	Na 4	1239	Na 3	1284	Na 5	1252	Na 5
Molten FeS (wt%)		1σ		1σ		1σ		1σ		1σ		1σ
Si	0.01	0.01	0.01	0.01	0.00	0.00	0.01	0.01	0.05	0.02	0.01	0.01
Ti	0.19	0.12	0.19	0.14	0.23	0.10	0.43	0.46	0.15	0.15	0.19	0.14
Al	0.01	0.01	0.00	0.00	n.a		0.00	0.00	0.00	0.01	0.00	0.00
Cr	0.33	0.09	0.42	0.21	n.a		0.37	0.24	0.44	0.3	0.42	0.21
Fe	62.11	0.26	60.19	0.57	56.13	8.13	60.8	1.6	60.52	0.87	60.19	0.57
Mn	0.19	0.05	0.18	0.07	0.61	1.04	0.17	0.02	0.13	0.04	0.18	0.07
Mg	0.01	0.01	0.03	0.02	2.59	4.90	0.13	0.01	0.11	0.04	0.03	0.02
Ca	0.00	0.01	0.00	0.01	0.17	0.34	0.02	0.01	0.01	0.01	0.00	0.01
Na	0.01	0.02	0.03	0.02	n.a		0.01	0.01	0.05	0.04	0.03	0.02
Ni	0.41	0.03	0.47	0.04	0.25	0.15	0.45	0.03	0.61	0.07	0.47	0.04
S	36.88	0.26	36.56	0.23	38.23	2.36	36.48	0.01	36.66	0.22	36.56	0.23
Total	100.14		98.09		98.21		98.87		98.74		98.09	

Run	1266	Na 5	1282	Na 5	1207	Na 7	1239	Na 1	1284	Na 5	1252	Na 5
Silicate (wt%)		1σ		1σ		1σ		1σ		1σ		1σ
SiO_2	60.3	2.06	58.13	1.97	60.04	26.23	60.62	6.06	58.05	2.23	59.47	0.90
TiO_2	0.00	0.01	0.06	0.03	0.00	0.02	0.06	0.01	0.00	0.01	0.01	0.01
Al_2O_3	0.29	0.15	0.5	0.25	0.11	0.01	0.26	0.03	1.07	1.78	0.22	0.04
FeO	0.59	0.20	0.28	0.10	0.19	53.18	0.30	0.03	0.64	0.24	0.10	0.02
MnO	0.02	0.02	0.01	0.01	0.02	0.01	0.00	0.00	0.01	0.01	0.01	0.01
MgO	39.18	1.57	37.38	1.64	40.00	0.02	39.92	3.99	36.69	4.27	38.8	0.96
CaO	0.92	0.06	0.31	0.11	0.09	0.03	0.15	0.01	0.61	0.99	0.09	0.03
Na_2O	0.06	0.08	0.01	0.01	0.00	0.00	0.00	0.00	0.04	0.05	0.01	0.00
K_2O	0.01	0.02	0.01	0.01	0.00	0.00	0.01	0.00	0.00	0.04	0.02	0.01
Ni_2O_3	0.00	0.00	0.02	0.02	0.01	0.79	0.00	0.00	0.02	0.02	0.01	0.02
SO_2	0.02	0.03	0.04	0.05	0.01	0.01	0.00	0.00	1.00	2.16	0.01	0.00
Total	101.40		96.74		100.47		101.30		98.17		98.75	

Run	1266	Na 9	1282	Na 10	1207	Na 4	1239	Na 3	1284	Na 3	1252	Na 5
Metal (wt%)		1σ		1σ		1σ		1σ		1σ		1σ
Si	0.01	0.02	0.01	0.03	1.72	0.73	0.44	0.61	2.9	0.19	3.25	2.06
Al	n.a		n.a		n.a		n.a		n.a		n.a	
Cr	0.03	0.03	0.03	0.02	n.a		n.a		n.a		n.a	
Fe	82.45	7.52	85.91	5.07	91.33	2.14	89.32	9.07	89.04	0.22	90.43	1.31
Mn	0.01	0.01	0.01	0.01	0.01	0.02	0.01	0.01	0.01	0.01	0.01	0.01
Mg	0.00	0.00	0.01	0.01	n.a		0.01	0.02	0.02	0.02	0.01	0.01
Ca	n.a		n.a		0.02	0.02	n.a		n.a		0.00	0.01
Ni	7.37	4.91	4.43	2.63	1.30	0.27	2.65	0.89	3.19	0.35	2.16	0.47
S	0.76	1.05	0.35	0.39	0.08	0.05	1.46	1.51	0.18	0.16	1.05	2.17
C	2.65	1.82	1.43	0.42	n.a		n.a		n.a		n.a	
Total	93.28		92.18		94.46		93.89		95.34		96.92	
C[a]	9.37		9.25		5.54		6.11		4.66		3.08	

Run	1266	Na 10	1282	Na 9	1207	Na 3	1239	Na 2	1284	Na 7	1252	Na 5
Silicate melt (wt%)		1σ		1σ		1σ		1σ		1σ		1σ
SiO_2	64.82	1.84	57.53	0.16	53.10	0.56	49.62	1.47	55.14	1.38	51.2	0.35
TiO_2	0.02	0.02	0.05	0.03	0.02	0.02	0.00	0.00	0.03	0.03	0.02	0.02
Al_2O_3	12.98	1.69	13.35	0.18	4.26	0.06	7.92	0.91	7.12	1.33	9.94	0.02
FeO	0.68	0.22	0.46	0.11	0.37	0.05	0.21	0.07	0.64	0.12	0.26	0.08
MnO	0.01	0.02	0.01	0.01	0.01	0.01	0.00	0.00	0.05	0.02	0.00	0.01
MgO	10.64	1.41	12.98	0.09	32.16	0.24	16.71	3.14	28.00	2.97	24.72	0.27
CaO	5.97	0.80	8.25	0.14	3.30	0.01	6.48	0.60	3.35	1.06	5.02	0.57
Na_2O	0.58	0.11	0.01	0.02	0.00	0.00	0.06	0.00	0.05	0.07	0.03	0.01
K_2O	0.10	0.04	0.00	0.01	0.00	0.00	0.00	0.00	0.03	0.03	0.02	0.01
Ni_2O_3	0.01	0.01	0.02	0.03	0.01	0.01	0.01	0.01	0.04	0.03	0.02	0.01
S	0.26	0.03	0.88	0.08	5.17	0.08	4.25	0.69	5.61	0.62	5.56	0.23
Total	96.33		93.54		98.39		85.25		100.06		96.08	

Na = Number of analyses

n.a Not analysed

a Maximum content calculated by difference from the total

O content in silicate and melt was estimated by stoichiometry

Table

Table 4: Minor and traces LA-ICP-MS composition of silicate melts and sulphides in ppm from experiments with CaS powders and associated Nernst oldhamites/melt REE partition coefficients.

Run	1250						1263						1208					
	Silicate melt		CaS		D		Silicate melt		CaS		D		Silicate melt		CaS		D	
	Na 4	1σ	Na 3	1σ		1σ	Na 5	1σ	Na 5	1σ		1σ	Na 6	1σ	Na 9	1σ		1σ
La	282	11.2	75	2.8	0.27	0.05	986	61.5	45	2.6	0.05	0.00	270	12.6	54	2.4	0.20	0.01
Ce	225	8.8	113	4.2	0.50	0.00	836	42.3	71	3.3	0.08	0.01	204	11	67	3.4	0.33	0.02
Pr	188	6.6	138	4.7	0.73	0.04	706	26.1	84	3.0	0.12	0.01	162	7.6	76	3.4	0.47	0.03
Nd	169	6.8	159	6.1	0.94	0.09	641	33.1	100	4.9	0.16	0.01	144	11.5	85	6.2	0.59	0.06
Sm	147	5.8	187	7.1	1.27	0.00	591	19.3	119	4.0	0.20	0.01	122	7.4	96	5.5	0.79	0.07
Eu	67	2.3	293	9.8	4.37	0.09	304	22.9	186	12.7	0.61	0.06	65.7	5.7	127	9.8	1.93	0.22
Gd	157	5.3	186	6.3	1.18	0.09	585	33.8	116	6.2	0.20	0.02	124	8.8	95	6.2	0.76	0.07
Tb	155	5.9	181	6.4	1.17	0.07	582	35.4	114	6.4	0.20	0.02	128	11.5	95	7.7	0.74	0.09
Dy	170	6.7	187	7.0	1.10	0.06	642	40.7	120	7.0	0.19	0.02	137	17.8	93	10.8	0.68	0.12
Ho	178	6.1	182	6.1	1.02	0.04	680	46.1	116	7.1	0.17	0.02	145	16.0	93	9.4	0.64	0.10
Er	188	6.4	166	5.6	0.88	0.03	703	46.5	106	6.4	0.15	0.01	153	10.8	88	5.7	0.57	0.06
Tm	202	6.6	150	4.8	0.74	0.01	774	38.8	989	4.6	0.13	0.01	163	15.8	81	7.1	0.50	0.07
Yb	145	5.1	217	7.4	1.50	0.08	620	19.3	129	4.1	0.21	0.01	110	10.5	111	9.6	1.01	0.13
Lu	238	7.9	124	4.0	0.52	0.02	885	29.2	81	2.7	0.09	0.00	192	20.5	73	7.1	0.38	0.05

Run	1240						1246						1305					
	Silicate melt		CaS		D		Silicate melt		CaS		D		Silicate melt		CaS		D	
	Na 5	1σ	Na 6	1σ		1σ	Na 6	1σ	Na 6	1σ		1σ	Na 6	1σ	Na 6	1σ		1σ
La	531	21.0	37	1.4	0.07	0.00	413	36.5	101	6.2	0.24	0.03	526	23.5	112	4.7	0.21	0.01
Ce	379	12.7	44	1.5	0.12	0.01	317	27.6	126	8.1	0.40	0.05	441	18.6	165	6.5	0.37	0.02
Pr	299	9.9	50	1.7	0.17	0.01	275	28.7	145	11.5	0.53	0.07	379	19.7	200	9.4	0.53	0.04
Nd	265	10.4	58	2.3	0.22	0.01	254	27.1	166	13.5	0.65	0.09	340	17.4	230	10.6	0.68	0.05
Sm	233	10.7	65	2.8	0.28	0.02	225	24.2	190	16.1	0.84	0.12	330	15.9	300	13.2	0.91	0.06
Eu	134	5.5	83	3.2	0.62	0.03	126	14.6	257	24.7	2.04	0.44	169	9.3	347	17.0	2.05	0.15
Gd	219	8.7	62	2.4	0.28	0.02	232	25.9	196	17.0	0.84	0.13	294	15.6	269	12.9	0.91	0.07
Tb	224	7.7	62	2.1	0.28	0.01	231	28.1	190	18.1	0.82	0.14	294	15.8	263	12.7	0.89	0.06
Dy	244	8.9	66	2.4	0.27	0.01	248	30.3	195	18.8	0.79	0.12	317	19.4	269	14.6	0.85	0.07
Ho	260	9.6	64	2.3	0.24	0.01	257	31.2	188	17.9	0.73	0.12	330	19.2	264	13.6	0.80	0.06
Er	269	8.4	59	1.9	0.22	0.01	268	33	178	16.9	0.66	0.11	345	18.5	243	11.7	0.70	0.05
Tm	297	9.1	55	1.7	0.19	0.01	280	38	162	16.8	0.58	0.11	360	20.1	219	10.9	0.61	0.05
Yb	226	7.7	68	2.3	0.30	0.01	221	30.2	222	24.1	1.00	0.22	289	18.7	270	15.3	0.93	0.08
Lu	333	10.7	47	1.5	0.14	0.01	323	47.2	145	15.8	0.45	0.08	400	24.2	186	9.9	0.47	0.04

Run	1244						1304					
	Silicate melt		CaS		D		Silicate melt		CaS		D	
	Na 6	1σ	Na 5	1σ		1σ	Na 4	1σ	Na 4	1σ		1σ
La	722	37.3	44	2.1	0.06	0.00	328	19.5	96	5.2	0.29	0.02
Ce	619	26.8	62	2.5	0.10	0.01	278	16.4	146	7.9	0.53	0.04
Pr	514	17.6	71	2.4	0.14	0.01	237	16.4	176	11.1	0.74	0.06
Nd	474	21.1	85	3.6	0.18	0.01	212	14.9	205	13.0	0.97	0.09
Sm	428	13.5	96	3.1	0.22	0.01	214	15.2	281	18.1	1.31	0.13
Eu	201	12.2	134	7.3	0.67	0.05	116	9.2	293	20.8	2.53	0.27
Gd	374	18.6	86	3.9	0.23	0.01	180	13.3	246	16.4	1.37	0.14
Tb	397	20	86	4.0	0.22	0.01	175	14.0	239	17.3	1.37	0.15
Dy	431	23.1	90	4.4	0.21	0.01	187	15.0	246	17.8	1.32	0.14
Ho	437	24.4	84	4.3	0.19	0.01	195	15.5	241	17.4	1.24	0.13
Er	471	25.7	80	4.0	0.17	0.01	202	16.3	225	16.4	1.11	0.12
Tm	506	22.0	74	3.0	0.15	0.01	212	18.6	206	16.3	0.97	0.12
Yb	407	12.8	98	3.1	0.24	0.01	176	15.7	245	19.7	1.39	0.17
Lu	538	17.6	57	1.8	0.11	0.00	241	22.8	178	15.1	0.74	0.09

Na = Number of analyses

Table 5: Minor and traces LA-ICP-MS composition of silicate melts and sulphide melts in ppm from experiments with FeS powders and associated Nernst molten FeS/silicate melt REE partition coefficients.

Run	1266						1282						1207					
	Silicate melt		Molten FeS		D		Silicate melt		Molten FeS		D		Silicate melt		Molten FeS		D	
	Na 2	1σ	Na 3	1σ		1σ	Na 3	1σ	Na 4	1σ		1σ	Na 3	1σ	Na 2	1σ		1σ
La	693	29.0	12	0.5	0.017	0.00	1848	80	63	2.0	0.034	0.00	1093	0.0	422	14.1	0.386	0.00
Ce	685	29.0	17	0.7	0.024	0.00	1778	105	56	1.8	0.032	0.00	1036	0.0	499	16.8	0.481	0.00
Pr	627	27.7	19	0.7	0.030	0.00	1679	119	73	2.3	0.043	0.00	1029	0.0	438	13.6	0.425	0.00
Nd	653	29.4	19	0.8	0.028	0.00	1798	145	56	2.0	0.031	0.00	1026	0.0	410	12.6	0.399	0.00
Sm	729	31.4	33	1.5	0.045	0.00	1924	144	78	2.6	0.041	0.00	1128	0.0	368	11.4	0.327	0.00
Eu	583	24.9	52	2.1	0.090	0.01	1122	104	137	4.3	0.122	0.01	905	0.0	596	18.6	0.658	0.00
Gd	927	44.4	23	1.0	0.024	0.00	2545	104	52	1.8	0.020	0.00	1319	0.0	200	6.2	0.152	0.00
Tb	947	45.2	27	1.1	0.029	0.00	2582	224	50	1.6	0.019	0.00	1475	0.0	142	4.4	0.097	0.00
Dy	1084	50.2	31	1.3	0.028	0.00	2813	238	52	1.7	0.018	0.00	1566	0.0	108	3.4	0.069	0.00
Ho	1117	53.8	27	1.0	0.024	0.00	2950	249	47	1.5	0.016	0.00	1718	0.0	68	2.1	0.039	0.00
Er	1116	50.9	23	1.0	0.021	0.00	3088	135	39	1.3	0.013	0.00	1717	0.0	43	1.4	0.025	0.00
Tm	1141	55.6	20	0.9	0.017	0.00	2936	176	30	1.0	0.010	0.00	1755	0.0	30	0.9	0.017	0.00
Yb	1096	51.5	39	1.6	0.036	0.00	2645	111	49	1.7	0.018	0.00	1678	0.0	83	2.6	0.050	0.00
Lu	1132	56.9	10	0.4	0.009	0.00	2859	113	18	0.6	0.006	0.00	1881	0.0	15	0.5	0.008	0.00

Run	1239						1284						1252					
	Silicate melt		Molten FeS		D		Silicate melt		Molten FeS		D		Silicate melt		Molten FeS		D	
	Na 3	1σ	Na 3	1σ		1σ	Na 5	1σ	Na 6	1σ		1σ	Na 5	1σ	Na 4	1σ		1σ
La	2527	92.2	139	91.4	0.055	0.04	599	21.3	14	0.5	0.024	0.00	768	30.9	209	110.0	0.272	0.14
Ce	2382	81.8	137	98.7	0.057	0.04	558	21.0	16	0.6	0.028	0.00	763	28.0	281	140.0	0.368	0.18
Pr	2300	75.7	111	95.2	0.048	0.04	499	20.5	13	0.6	0.026	0.00	729	25.0	296	150.0	0.406	0.21
Nd	2386	84.5	127	104.3	0.053	0.04	553	22.4	13	0.6	0.024	0.00	752	29.1	251	134.0	0.334	0.18
Sm	2636	88.0	133	111.5	0.051	0.04	598	24.5	12	0.5	0.019	0.00	825	29.0	244	129.0	0.296	0.16
Eu	1974	65.4	145	146.9	0.074	0.07	543	22.9	15	0.6	0.027	0.00	480	16.7	287	158.0	0.598	0.33
Gd	3211	108.7	97	76.0	0.030	0.02	786	32.3	7	0.3	0.009	0.00	1054	37.8	148	75.2	0.140	0.07
Tb	3383	116.6	89	63.2	0.026	0.02	826	33.0	5	0.2	0.006	0.00	1093	40.6	113	57.5	0.103	0.05
Dy	3687	124.5	92	60.8	0.025	0.02	923	34.7	4	0.2	0.004	0.00	1190	42.6	79	41.9	0.067	0.04
Ho	4057	137.2	86	47.6	0.021	0.01	1005	37.7	3	0.1	0.003	0.00	1282	46.1	48	24.7	0.037	0.02
Er	4023	137.0	68	34.5	0.017	0.01	1005	39.4	2	0.1	0.002	0.00	1283	46.5	26	13.2	0.020	0.01
Tm	4226	145.4	48	26.9	0.011	0.01	1050	38.8	1	0.1	0.001	0.00	1335	49.4	15	7.5	0.011	0.01
Yb	3947	141.1	136	59.3	0.035	0.02	996	37.4	3	0.1	0.003	0.00	1222	48.0	51	25.9	0.042	0.02
Lu	4381	155.1	18	13.7	0.004	0.00	1186	43.3	1	0.0	0.000	0.00	1417	54.7	5	2.5	0.003	0.00

Na = Number of analyses

Table

Table 6: D/D* ratios calculated for oldhamite/melt partitioning experiments.

Run	1244	1263	1250	1240	1305	1304	1246	1208
La	0.87	0.82	0.80	0.86	0.85	0.84	0.88	0.85
Ce	0.90	0.91	0.90	0.87	0.90	0.90	0.93	0.89
Pr	0.90	0.90	0.92	0.9	0.90	0.88	0.91	0.91
Nd	1.06	1.06	1.06	1.06	1.04	1.03	1.03	1.05
Sm	1.08	1.07	1.12	1.06	1.09	1.07	1.08	1.11
Eu	2.98	3.09	3.67	2.20	2.31	1.90	2.48	2.60
Gd	1.00	0.98	0.98	1.00	1.00	1.00	1.01	1.01
Tb	0.99	1.00	0.99	0.98	1.00	1.00	1.00	1.00
Dy	1.00	1.01	1.00	1.01	0.99	1.00	1.00	0.97
Ho	1.02	1.02	1.03	1.01	1.02	1.01	1.01	1.01
Er	1.03	1.03	1.03	1.03	1.03	1.01	1.02	1.02
Tm	1.04	1.02	1.03	1.01	1.01	1.01	1.01	1.02
Yb	2.14	2.11	2.65	2.03	1.92	1.77	2.13	2.57
Lu	1.09	1.09	1.09	1.11	1.11	1.08	1.09	1.12

Figure
Click here to download high resolution image

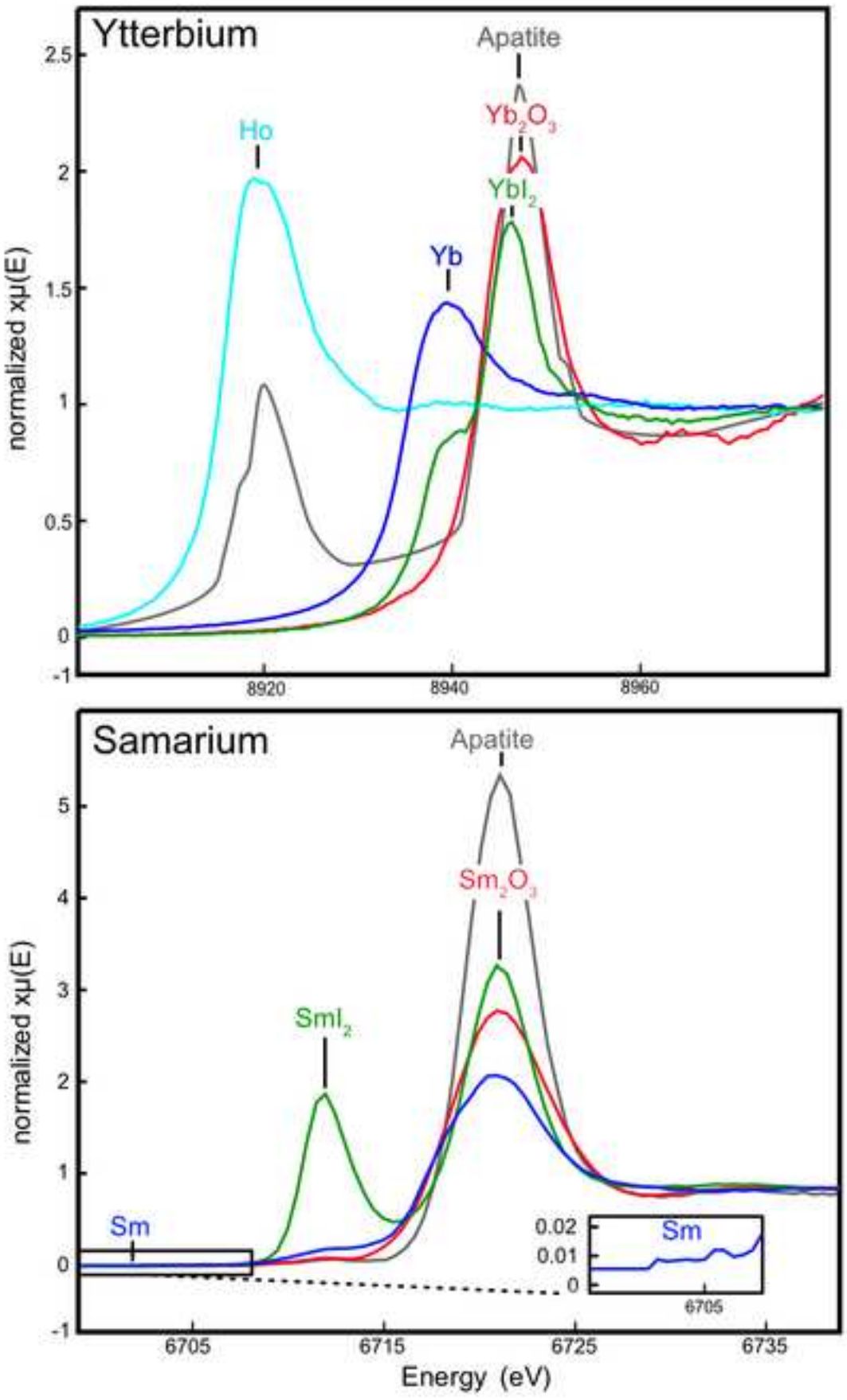

Figure

Click here to download high resolution image

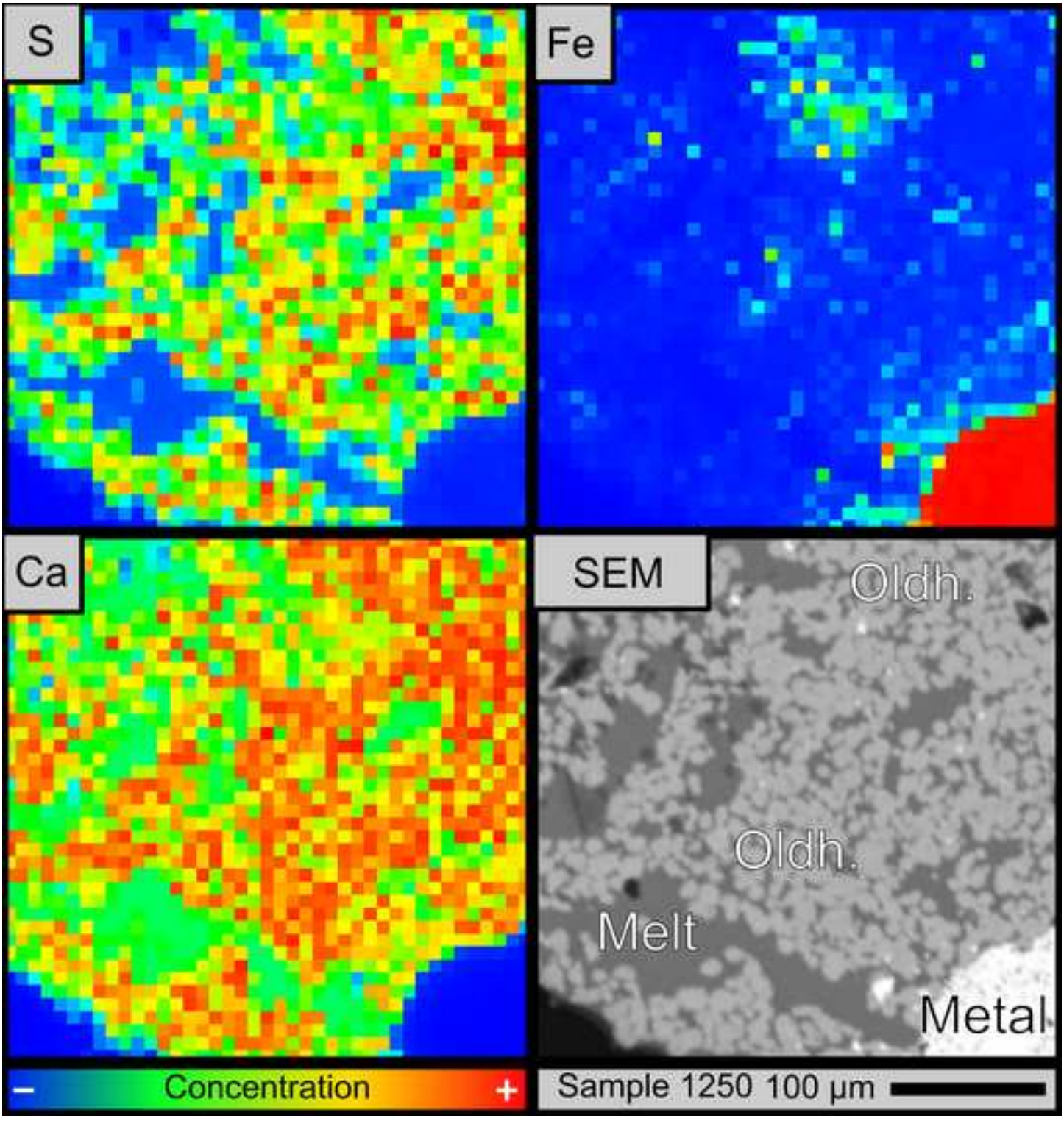

Figure

Click here to download high resolution image

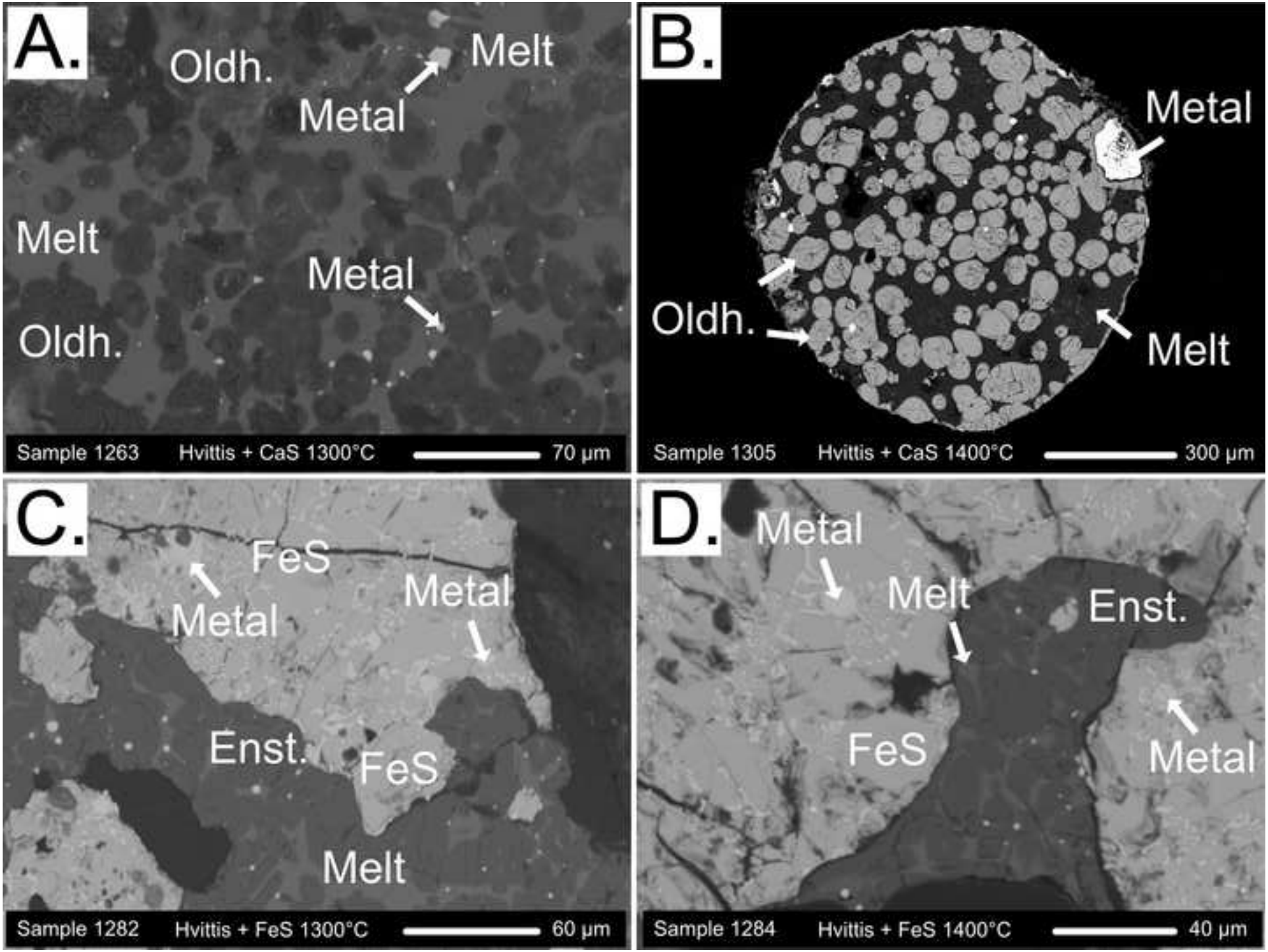

Figure

Click here to download high resolution image

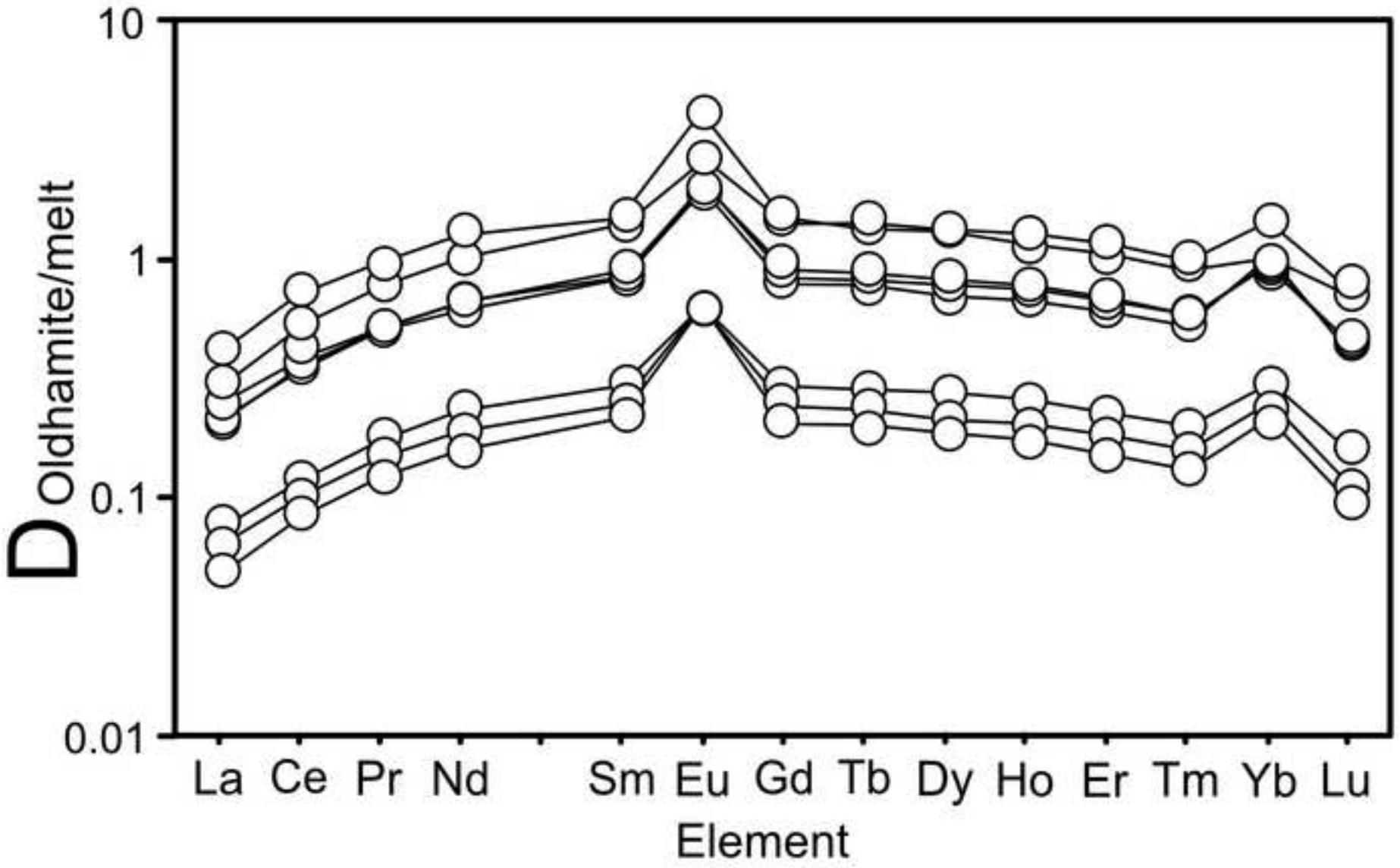

Figure

Click here to download high resolution image

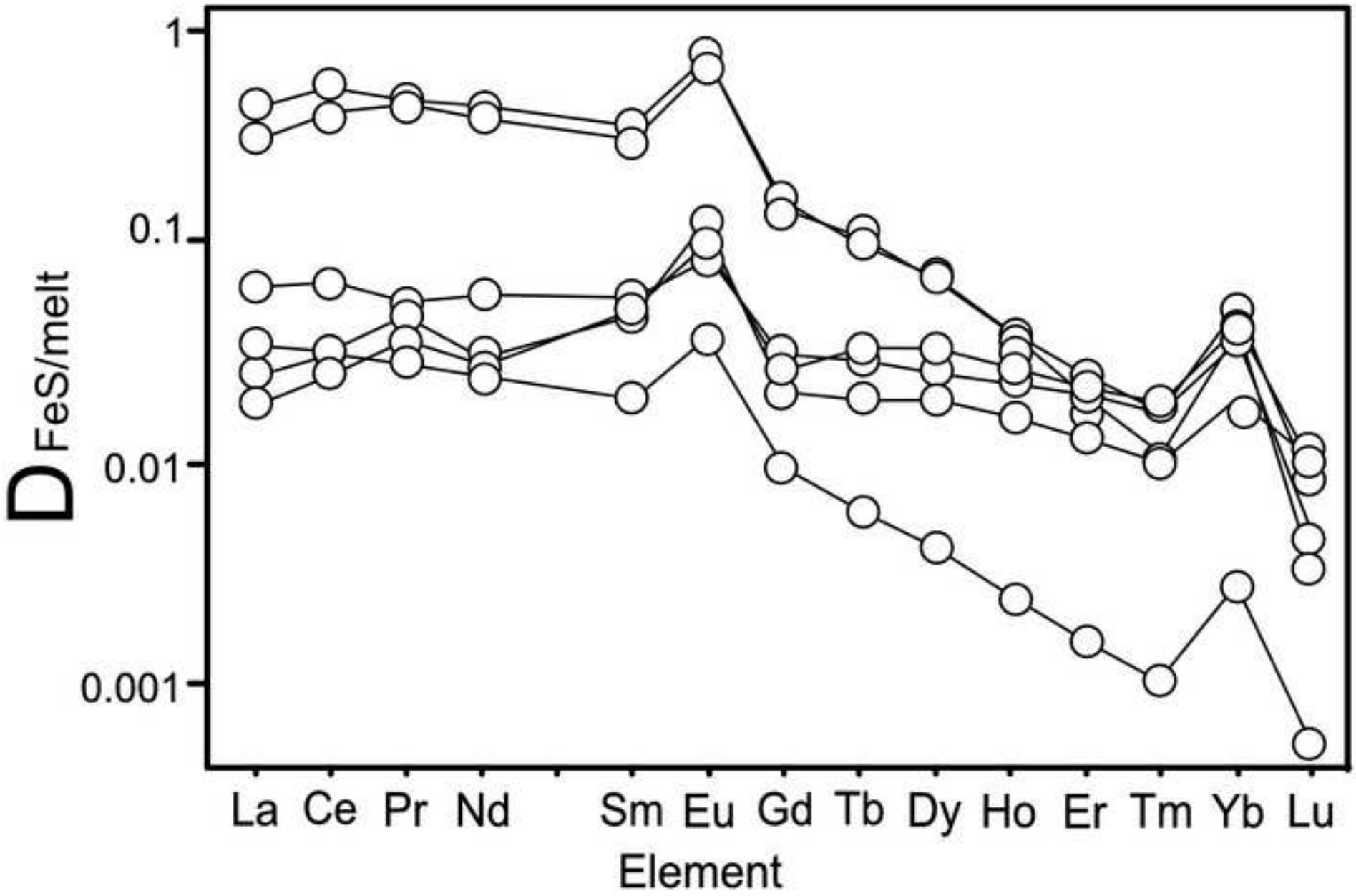

Figure

Click here to download high resolution image

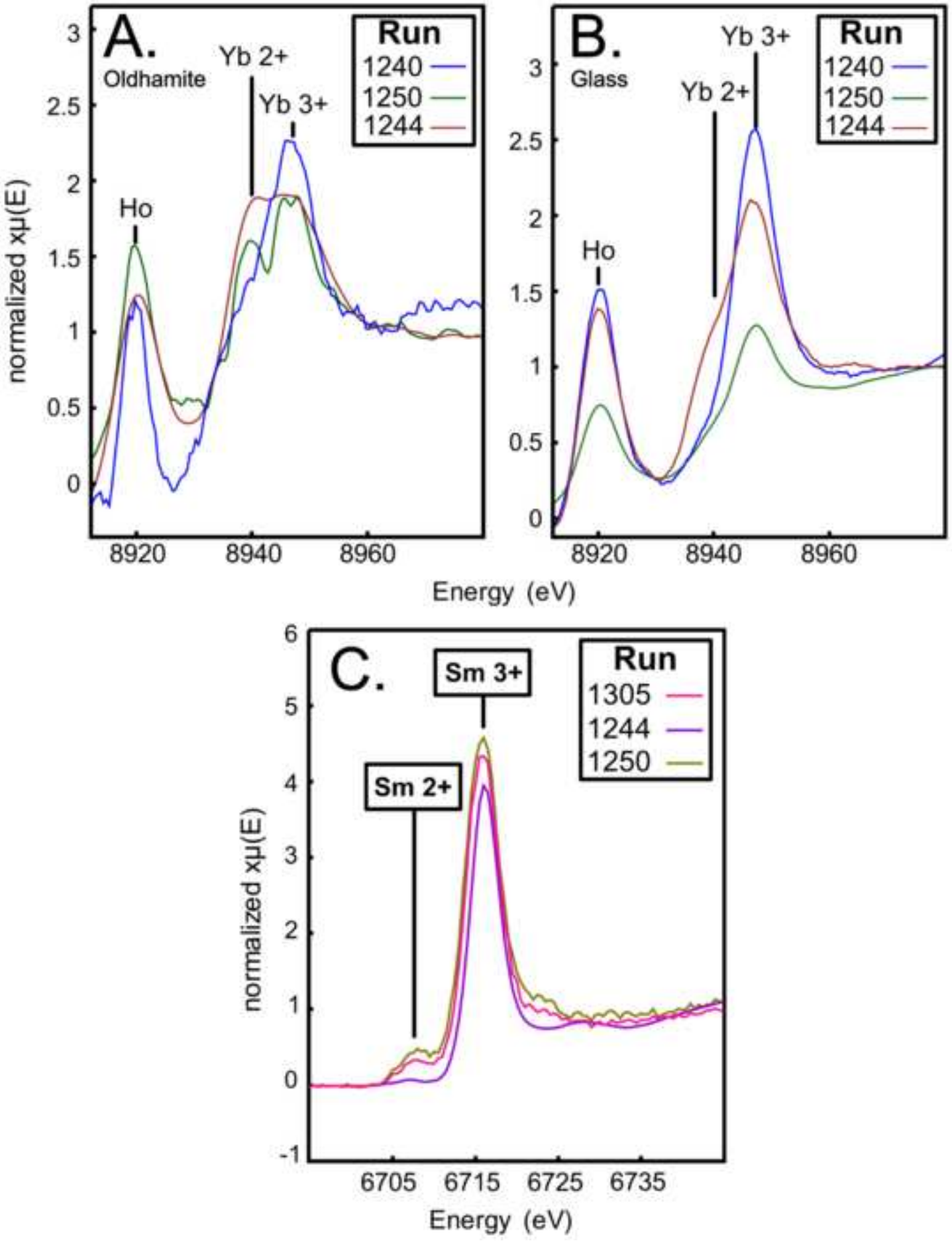

Figure

Click here to download high resolution image

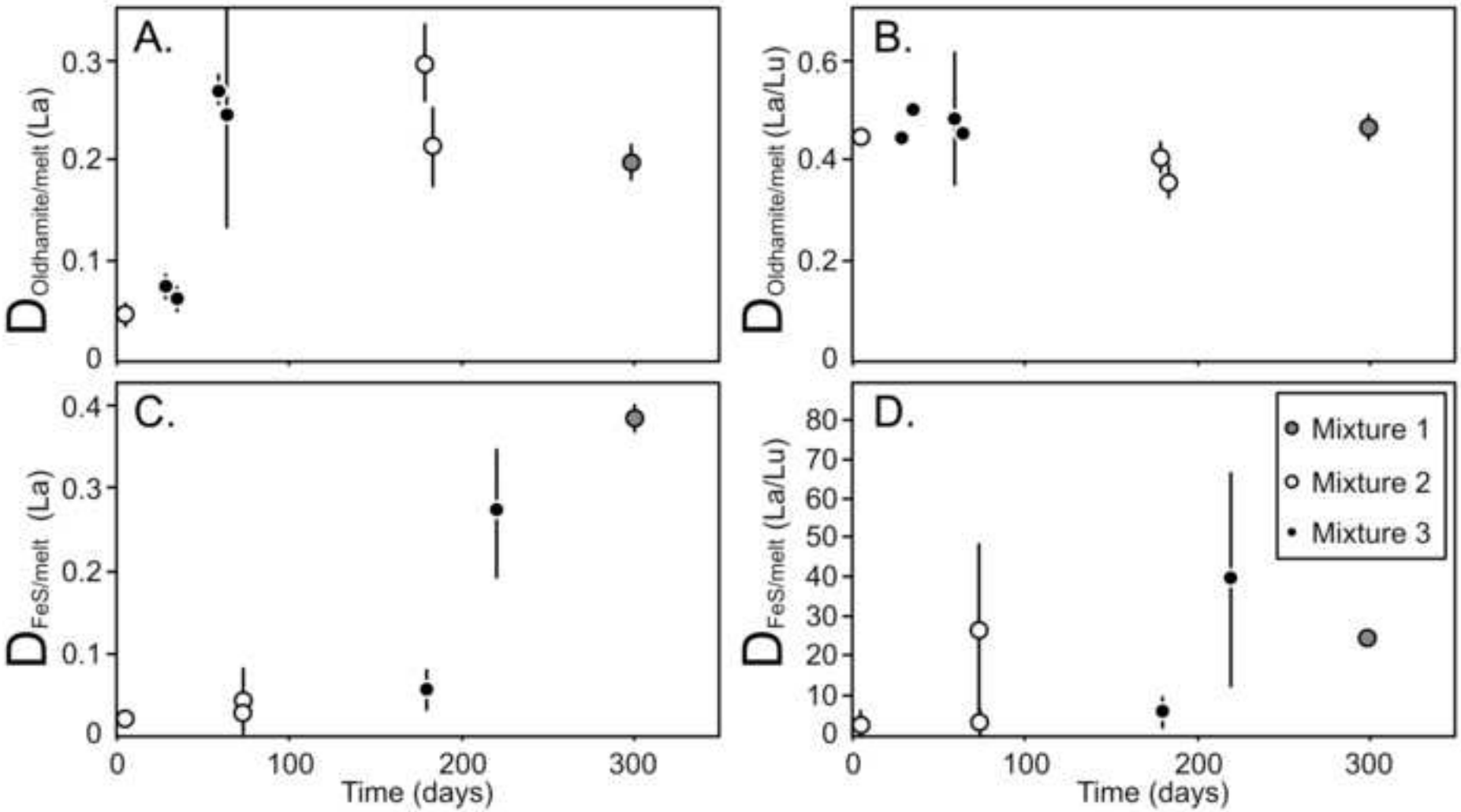

Figure
Click here to download high resolution image

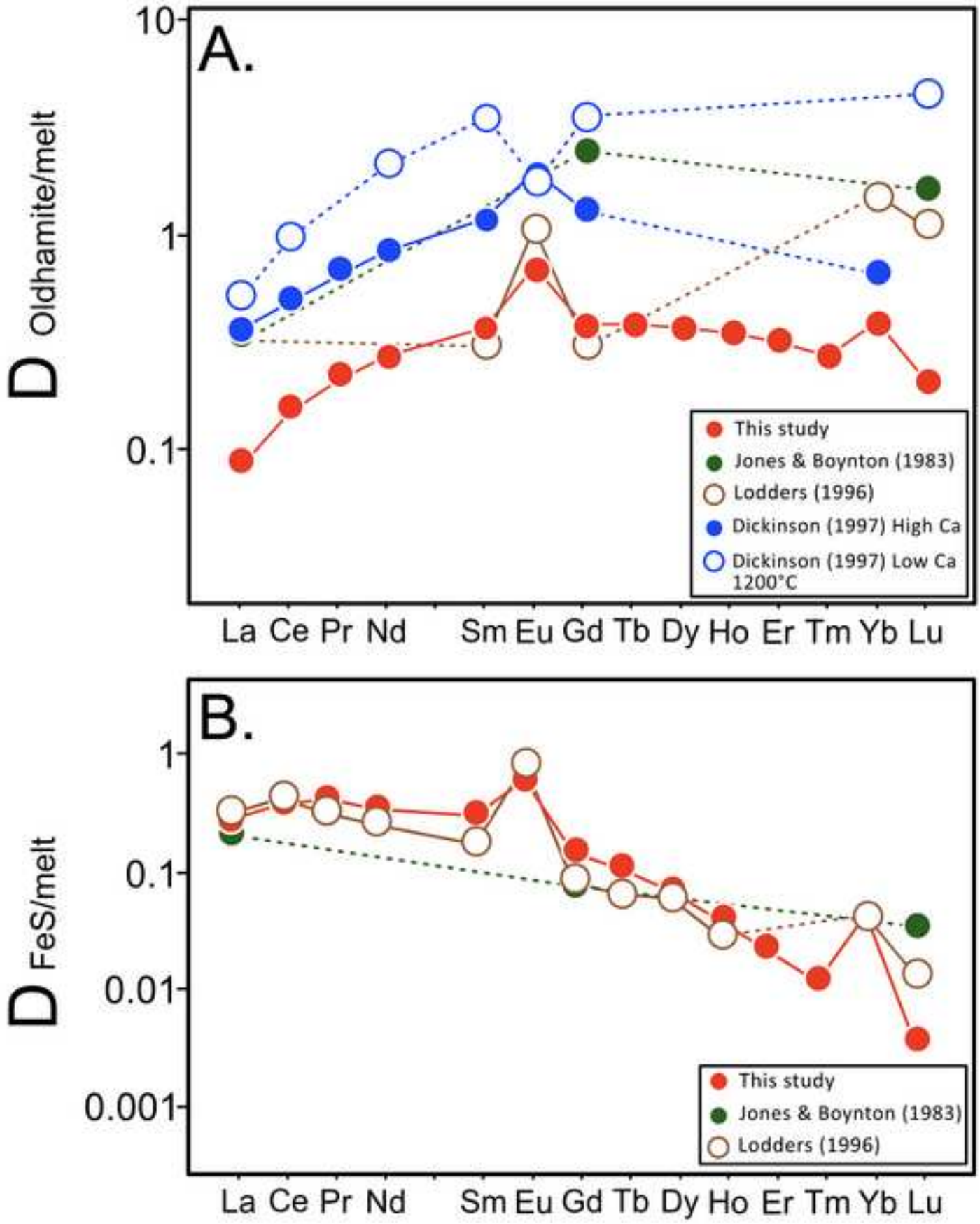

Figure
Click here to download high resolution image

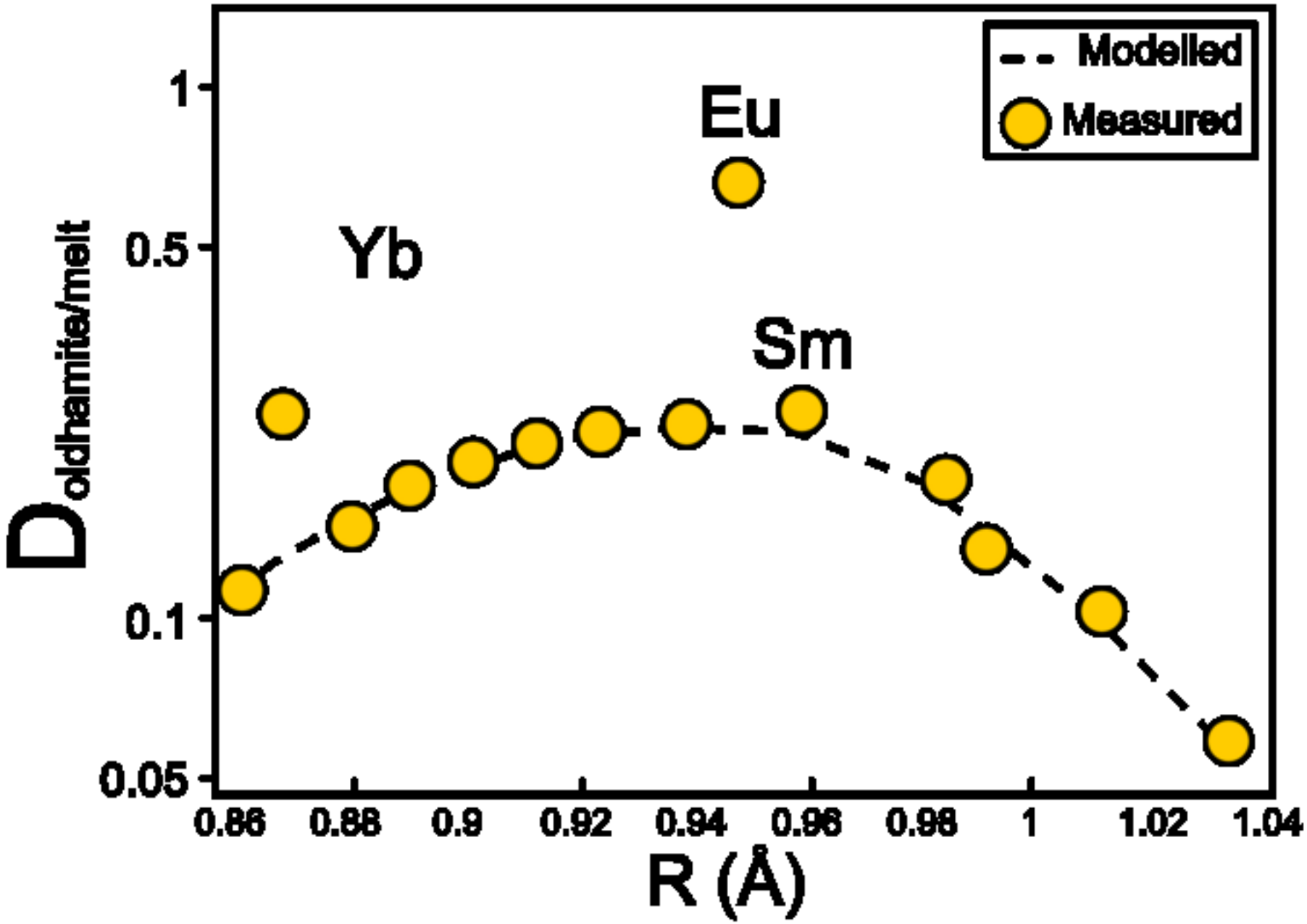

Figure
Click here to download high resolution image

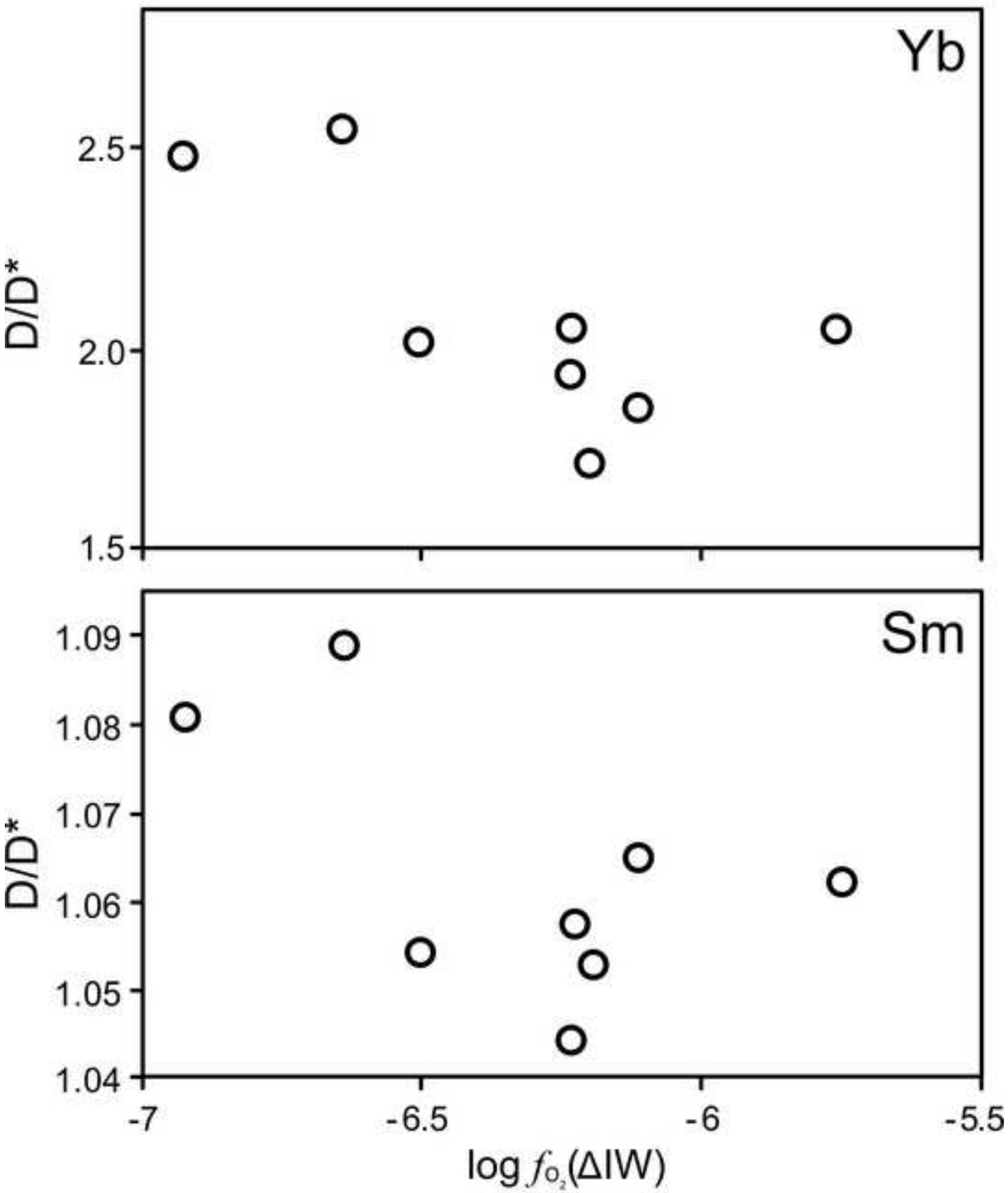

Figure

Click here to download high resolution image

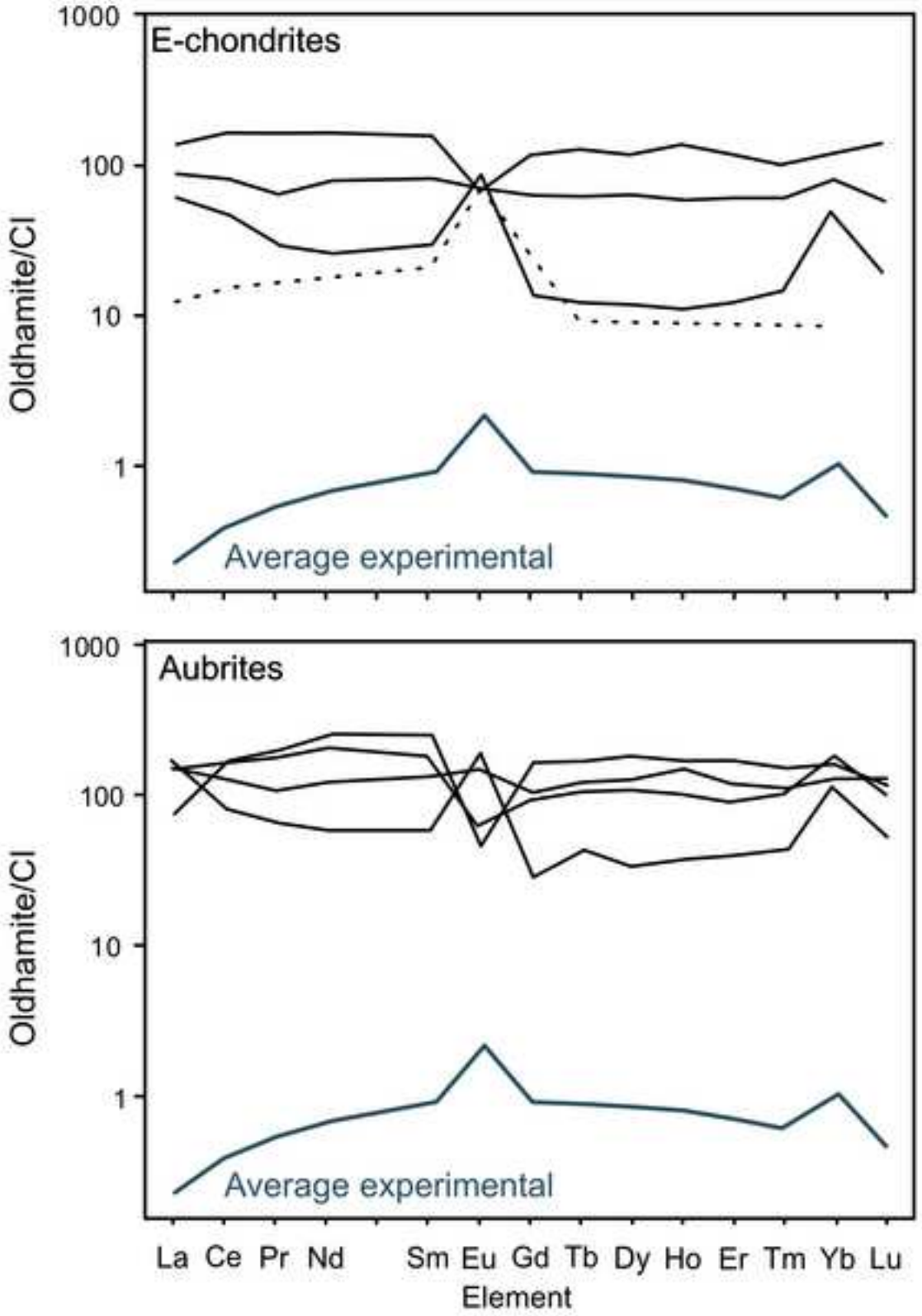

Electronic Annex

Click here to download Electronic Annex: Supplementary_table_1.pdf

Electronic Annex

Click here to download Electronic Annex: Supplementary_table_2.pdf